

Die approbierte Originalversion dieser Diplom-/Masterarbeit ist an der Hauptbibliothek der Technischen Universität Wien aufgestellt (<http://www.ub.tuwien.ac.at>).

The approved original version of this diploma or master thesis is available at the main library of the Vienna University of Technology (<http://www.ub.tuwien.ac.at/englweb/>).



TECHNISCHE  
UNIVERSITÄT  
WIEN  
Vienna University of Technology

## Masterarbeit

# Synthesis and Comparison of Catalysts to Enhance the Hydrogen Yield during Biomass Gasification

Ausgeführt zum Zwecke der Erlangung des akademischen Grades eines

Diplom-Ingenieur

am Institut für Chemische Verfahrenstechnik der TU Wien,  
unter Anleitung von

Univ.Prof. Dipl.-Ing. Dr.techn. Hermann HOFBAUER,  
und

Dipl.-Ing. Dr.techn. Christoph PFEIFER,

ausgeführt durch

**Stefan KOHLEGGER**

Winkelfeldsteig 62  
6020 Innsbruck  
Matrikelnummer 0625928

Wien, am 12.6.2012

# Kurzfassung

Wasserstoff gilt als attraktiver Brennstoff in der Energiebereitstellung der Zukunft und als mögliche Lösung für die schwindenden fossilen Ressourcen, und die mit deren Verbrennung verbundenen Umweltprobleme, wird jedoch momentan selbst zum Großteil aus fossilen Quellen gewonnen. Die Biomassevergasung stellt eine interessante Technologie der Wasserstoffherstellung aus erneuerbaren Energieträgern dar. Die Verwendung von Katalysatoren im Vergasungsprozess ist eine weitverbreitete Möglichkeit zur Erhöhung der Wasserstoffausbeute bzw. -selektivität, und eine notwendige Maßnahme zur Steigerung der Konkurrenzfähigkeit des Verfahrens, bedarf jedoch - aufgrund der im Reaktor vorherrschenden, hohen Temperaturen ( $> 800\text{ °C}$ ) und Feuchten - hoch-stabiler Materialien. Siliziumkarbid (SiC) könnte aufgrund seiner einzigartigen Eigenschaften, ein geeignetes Trägermaterial für Katalysatoren in diesem Zusammenhang sein.

In der vorliegenden Arbeit wurden ein neuartiger Nickel-Cobalt-Katalysator auf mesoporösem SiC, sowie ein Nickel-Cobalt Katalysator auf mesoporösem Silika (SBA-15), als Referenzmaterial, mit einer Beladung von 10 m% und einem Nickel-Kobalt-Verhältnis von 1:2 hergestellt, und auf ihre Aktivität bzw. Selektivität in der  $\text{H}_2$ -Herstellung während der Vergasung von Methylzellulose, welche als Biomasseersatz gewählt wurde, getestet. Die Trägermaterialien SBA-15 bzw. SiC wurden über das *liquid crystal templating*- bzw. *nano casting* Verfahren synthetisiert, wobei SBA-15 als Vorlage für die Synthese des mesoporösen SiC verwendet wurde. Die aktiven Metalle Nickel und Kobalt wurden über Kapillarimprägnierung in die Trägermaterialien eingebunden. Die Vergasung wurde in einem Laborreaktor, bestehend aus einer Thermogravimetrieanalyse und einem Massenspektrometer, unter Argon, durch Aufheizung auf  $800\text{ °C}$  realisiert. Die Charakterisierung der Katalysatoren erfolgte durch Verfahren der physikalischen- und chemischen Adsorption, Methoden der Röntgenbeugung, sowie durch Raster- und Transmissionselektronenmikroskopie.

Die Zugabe der mesoporösen Katalysatoren zur Vergasung führte sowohl für  $\text{NiCo}_2/\text{SBA-15}$ , als auch für  $\text{NiCo}_2/\text{SiC}$  zu einer signifikanten Steigerung der Wasserstoffausbeute bzw. -selektivität.  $\text{NiCo}_2/\text{SiC}$  bzw.  $\text{NiCo}_2/\text{SBA-15}$  steigerten die Wasserstoffausbeute um das mehr als 6- bzw. 14-fache, verglichen mit der Vergasung der reinen Zellulose. Der Anteil an Wasserstoff im Produktgas stieg von 1.0 vol% (reine Zellulose) auf 5.3 (NiCo<sub>2</sub>/SiC) bzw. 8.2 vol% (NiCo<sub>2</sub>/SBA-15).

# Abstract

Hydrogen is considered as a promising energy carrier to meet prospective requirements in the global energy supply and get away from receding fossil resources and the associated environmental problems. An interesting pathway of producing hydrogen from renewables, rather than from fossil fuels, which are currently most commonly used, is the steam gasification of biomass. In order to increase the selectivity of H<sub>2</sub> during biomass gasification, and thus make it more competitive with current techniques for large-scale hydrogen production, various catalysts can be introduced into the process. The high temperatures (> 800 °C) and humidity required for gasification processes require highly mechanically, thermally and hydrothermally stable catalysts. In this context silicon carbide (SiC) is an interesting support material for catalysts.

In this work a novel, mesoporous SiC-supported Ni-Co catalyst as well as a mesoporous silica (SBA-15) supported catalyst, were synthesized via incipient wetness impregnation. Both catalysts had a total metal loading of 10 wt% and a nickel-to-cobalt ratio of 1:2. The catalysts were tested for their selectivity and activity in H<sub>2</sub> production from the gasification of methyl cellulose, which was chosen as the biomass substitute. The experiments were accomplished in a thermogravimetric analyzer coupled with a mass spectrometer. The samples were heated under argon up to 800 °C at a heating rate of 40 °C/min. The supports, SBA-15 and SiC, were prepared using liquid crystal templating and a nanocasting process, respectively. SBA-15 was used as a template for the synthesis of SiC. The blank support materials and the catalysts were characterized by N<sub>2</sub> physisorption, X-ray diffraction, small angle X-ray scattering as well as scanning and transmission electron microscopy. The catalysts were also characterized by H<sub>2</sub> chemisorption.

Both, SiC- and SBA-15-supported Ni-Co catalysts significantly increased the H<sub>2</sub> yield and selectivity of the gasification of cellulose. NiCo<sub>2</sub>/SiC elevated the H<sub>2</sub> yield by more than six times and NiCo<sub>2</sub>/SBA-15 by more than 14 times, compared to the output obtained when no catalyst was present. The share of H<sub>2</sub> in the product gas distribution increased from 1.0 vol% without a catalyst, to 5.3 vol% and 8.2 vol% for NiCo<sub>2</sub>/SiC and NiCo<sub>2</sub>/SBA-15.

# Acknowledgements

First of all, I would like to thank Prof. Andrew Harris and the University of Sydney for giving me the opportunity to realize this work at the Laboratory for Sustainable Technologies at Sydney Uni, and for sponsoring my visa application.

I would also like to give my thanks to Prof. Hermann Hofbauer who facilitated my exchange on behalf of the Institute of Chemical Engineering of the Vienna University of Technology and supported this work as my supervisor.

I'm very grateful to Dr. Christoph Pfeifer who pulled all strings to establish the initial contact with Dr. Andrew Harris and thus made this exchange even possible. I furthermore would like to thank him for his steady scientific and personal support and his patience during all our Skype-discussions.

I'd like to thank Dr. Tamara Church and Dr. Ming Zhao, who supervised my work at the Laboratory for Sustainable Technologies, and who shared their expertise with me. I'm thankful for all the time they sacrificed to help me with my experiments and all the help and advice they supplied.

I also want to mention Meilina Widyawati, who shared all her knowledge about the synthesis of mesoporous silicon carbide with me, and Victor Lo who made a lot of effort helping me with the microanalysis of my various samples.

I want to acknowledge the financial support I received from the International Office as well as the deanery of the Institute of Mechanical Engineering of the Vienna University of Technology.

I'm especially grateful for my parents, Monika and Alfred, who always supported my studies in Vienna, my trip to Sydney and who allowed me to acquire a broad education. Not forgetting my brothers, Markus and Mike, who were on hand with help and advice whenever needed.

Finally, I want to thank my girlfriend Julia for supporting my trip to Australia and following me to Sydney after finishing her studies in Vienna. I'm thankful for her patience during countless conversations about this work and the associated issues, her steady support even during stressful times and for making my time in Australia even better.

# Contents

<b>1 Aim of the work</b>	<b>8</b>
1.1 Background . . . . .	8
1.2 Aim and methodology . . . . .	8
<b>2 Introduction</b>	<b>10</b>
2.1 The role of hydrogen in the future . . . . .	10
2.1.1 A general energy outlook . . . . .	10
2.1.2 Hydrogen: status and outlook . . . . .	12
2.2 An overview of hydrogen production . . . . .	15
2.2.1 Hydrogen from fossil fuels . . . . .	15
2.2.2 Hydrogen from biomass . . . . .	18
2.2.3 Short overview of the cost of hydrogen production . . . . .	20
2.3 Hydrogen from biomass gasification . . . . .	21
2.3.1 Fundamentals . . . . .	21
2.3.2 Purification processes . . . . .	24
2.4 Catalysts in biomass gasification processes . . . . .	29
2.4.1 Fundamentals . . . . .	29
2.4.2 Catalysts to enhance the H <sub>2</sub> yield during biomass gasification . . .	31
2.4.3 Catalyst support materials . . . . .	33
<b>3 Experimental</b>	<b>35</b>
3.1 Synthesis of catalyst . . . . .	35
3.1.1 Synthesis of SBA-15 . . . . .	35
3.1.2 Synthesis of SiC . . . . .	37
3.1.3 Incorporation of metals into substrates . . . . .	40
3.2 Characterization of catalysts . . . . .	42
3.2.1 Surface area, pore volume and pore size distribution . . . . .	42
3.2.2 Crystalline structure and chemical compound . . . . .	43
3.2.3 Surface morphology and pore structure . . . . .	44
3.2.4 Active surface area . . . . .	45

## Contents

3.3	Testing of Catalysts . . . . .	46
3.3.1	Apparatus . . . . .	46
3.3.2	Experiment . . . . .	47
3.3.3	Evaluation . . . . .	48
<b>4</b>	<b>Results and discussion</b>	<b>49</b>
4.1	Characterization of support materials and catalysts . . . . .	49
4.2	Catalyst testing . . . . .	56
4.2.1	H <sub>2</sub> yield . . . . .	57
4.2.2	H <sub>2</sub> generation . . . . .	58
4.2.3	H <sub>2</sub> selectivity . . . . .	65
<b>5</b>	<b>Conclusion and outlook</b>	<b>66</b>
5.1	Conclusion . . . . .	66
5.2	Outlook . . . . .	67
<b>6</b>	<b>Nomenclature</b>	<b>68</b>

# 1 Aim of the work

## 1.1 Background

A rising energy demand, together with receding fossil fuel reserves and growing environmental problems, make finding alternative, preferably sustainable, energy sources and the development of effective technologies key issues for our society. Hydrogen is considered a potential energy carrier for the future, as it can be produced from a variety of feedstocks, including fossil fuels and renewables, and can be cleanly and efficiently converted into electrical energy using fuel cells, where it co-produces nothing but water and heat. An attractive, sustainable technology for producing hydrogen from renewables is the steam gasification of biomass, which is considered as the renewable energy source with the highest potential to contribute to prospective energy needs [1]. The main problem with this technology, apart from economic aspects, is the limited share of hydrogen (depending on the applied system and used catalysts, between about 5 to 60 vol% have been accomplished [2]) in the product gas measured against the purity of hydrogen required for a direct use in fuel cells (proton exchange membranes require a purity of hydrogen at > 99.9% [3]). This indicates the need of costly downstream purification processes to obtain high-purity hydrogen.

A possible solution is the use of effective catalysts directly in the reactor. This could significantly enhance the hydrogen yield and selectivity during the gasification process, decrease the requirements for downstream gas cleaning and thus make the hydrogen production from biomass gasification more competitive among currently used techniques, such as steam methane reforming, coal gasification or electrolysis. The harsh environment used in steam gasification processes (temperatures > 800 °C, high humidity) puts high requirements on the mechanical, thermal and hydrothermal properties of the applied catalysts. In this context, mesoporous silicon carbide (SiC) seems to be an interesting support material for catalysts [4].

## 1.2 Aim and methodology

The aim of this work is to synthesize a mesoporous-SiC-supported nickel-cobalt-catalyst and examine its impact on the hydrogen yield and selectivity during the gasification of

## *1 Aim of the work*

methyl cellulose (a biomass substitute) in a lab-scale reactor. For this purpose a mesoporous silica, known as SBA-15, which has been well-investigated as a catalyst support in the hydrogen production [5, 6, 7], is initially synthesized via a liquid crystal templating method and subsequently used as a template for the synthesis of mesoporous SiC using a nanocasting process. The SiC support is then impregnated with nickel and cobalt precursors, which are reduced to the active metals nickel and cobalt. The catalyst is then mixed with cellulose which is gasified in a lab-scale reactor (thermogravimetric analyser coupled with a mass spectrometer). For comparison, a sample of pure cellulose, as well as a sample of cellulose mixed with the silica-supported catalyst, are also tested in the reactor. The structures of both, the support materials and the catalysts are examined using X-ray diffraction methods (XRD, SAXS), N<sub>2</sub> physisorption (BET surface area, BJH pore size distribution) and transmission and scanning electron microscopy (TEM, SEM). The catalysts are further characterized using H<sub>2</sub> chemisorption.

The introduction gives a short outlook on the future of hydrogen as a fuel, an overview of the various hydrogen-producing technologies, with an emphasis on hydrogen production from biomass gasification and an overview of catalysts used to enhance the hydrogen yield during biomass gasification.

## 2 Introduction

### 2.1 The role of hydrogen in the future

#### 2.1.1 A general energy outlook

According to the statistics published by the International Energy Agency, IEA, in October 2011, the global consumption of primary energy came to 12 150 Mtoe<sup>1</sup> (510 EJ) in 2009, and fossil fuels covered more than 80% of this demand, as seen in Figure 2.1 [8]. Although this is a decline compared to energy use in 2008, possibly due to the economical crises at that time, the global demand for energy is on a rising curve. In 2010 the world's consumption of energy increased by about 5% compared to 2009 [9]. Recent energy outlooks, such as the *Energy Outlook 2011* from the IEA [10], the *Energy Outlook 2030* from BP [11] and *A View to 2040* from Exxon [12] furthermore agree that the demand on primary energy and the associated emission of greenhouse gases will constantly increase over the following decades.

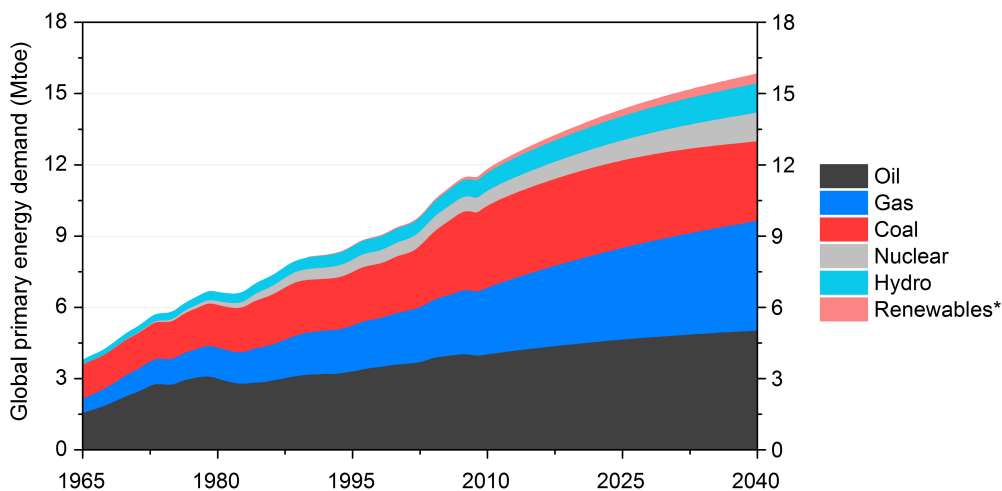


**Figure 2.1** Global primary energy demand in Mtoe between 1965-2040 based on Exxon's energy outlook 2011 [12]. (\* including biofuels)

<sup>1</sup>Mtoe, which stands for *Mega tonnes oil equivalent*, is a unit used in the context of energy consumption. 1 Mtoe is equivalent to  $41.868 \cdot 10^{12}$  J.

## 2 Introduction

The IEA described three possible future scenarios based on three different initial situations. The *New Policy Scenario*, which is the central scenario in the outlook and the one considered in this work, assumes that recent government policy commitments are to be fully implemented in a cautious manner. The two other scenarios are the *Current Policies Scenario*, which supposes no new policies are added to those in place as of mid-2011, and the *450 Scenario*, which works backwards from the international goal of limiting the long-term concentration of greenhouse gases in the atmosphere to 450 ppm CO<sub>2</sub>-equivalents, implying an average temperature rise of not more than 2 °C by 2030. The outlooks published by BP and Exxon do not take government policies as given, but make judgements on the probability of future policy developments and impacts, and therefore lie between the IEA's New and Current Policy Scenarios.

Despite that the outlooks differ from each other in some areas, possibly due to different judgements on market factors, technology improvements and governmental policies and the different time periods considered, they share many similar core findings:

- Although the rate of increase of the global primary demand for energy slows down over the coming decades, the total energy demand increases by more than 35%. (Figure 2.1). The increase is driven by the expected growth in population and the growing global economy.
- Non-OECD countries (China, India, Indonesia, Brazil, etc.) cause about 90% of the rising energy demand.
- Energy-related CO<sub>2</sub> emissions increase by about 20%, which is in fact a slowdown, but nevertheless leads to a rise of 3.5 °C in the average global temperature by 2030 [10] and to associated environmental issues.
- The world demand grows for all energy sources. Renewables, before natural gas, grow faster than any other energy form (Figure 2.1).
- The global energy mix changes and becomes more diverse. The share of renewables increases from about 3 to more than 16%, whereas the amount of fossil fuels declines from about 80 to 75% but will still represent the lion's share. For the first time, non-fossil fuels are the major sources of supply growth (Figure 2.1).
- Natural gas plays an increasingly important role in the global energy economy (especially in meeting the rising electricity demand). Among fossil fuels, it is the only fuel to increase its share in the global mix.
- Power generation is the fastest-growing energy sector. It is the driving force for coal demand and the installation of nuclear power plants.

## 2 Introduction

The outlooks furthermore agree that there are fundamental needs to expand and diversifying supplies, improve efficiency and addressing environmental issues, and that huge investments are required to meet these challenges.

### 2.1.2 Hydrogen: status and outlook

Current annual hydrogen production is 65 million tones (8 EJ) per year, which is less than 2% of the global primary energy supply [13]. Almost all of it is produced from fossil fuels through natural gas reforming or coal gasification (see Section 2.2), and is used industrially for non-energy purposes. The main industrial applications of hydrogen are:

- Conversion of heavy petroleum fractions into lighter ones in the oil and chemical industries.
- Synthesis of ammonia via the *Haber Process* in the fertilizer industry.
- Saturation of unsaturated fats and oils in the food industry.
- As a reducing agent in the steel industry.

Although it doesn't play a big role in today's energy economy, there is a growing interest in hydrogen as an energy carrier, especially together with fuel cells that convert the chemical energy of  $H_2$  into electricity. Particularly in automotive industries this technology is considered to be a promising alternative to current drive systems, which use petroleum-based fuels at fairly low efficiencies limited by the *Carnot Process*. Fuel Cell Vehicles working at higher efficiencies (fuel cells can theoretically reach 100% efficiency [14]) would need less energy input, and would contribute to reduce greenhouse gas emissions, as water and heat are the only products from the reaction taking place in an ideal  $H_2$  fuel cell. Even if the  $H_2$  was produced from fossil fuels and the emission of greenhouse gases during the synthesis was considered, hydrogen processed in fuel cells would be advantageous due to better exploitation of the energy. According to a Well-to-Wheel<sup>2</sup> simulation analysis conducted by General Motors, a fuel cell electric vehicle running on compressed gaseous hydrogen produced from natural gas could use about 40% less energy and emit 45% less greenhouse gasses per mile travelled than an internal combustion vehicle does [15].

Taking in account that hydrogen can also be produced from renewables, such as biomass or water (see Section 2.2), which must be the goal, makes these cars even more promising. In summary, the advantages of hydrogen as an energy carrier are [16, 17, 13, 14]:

---

<sup>2</sup>Well-to-Wheel is an analysis methode used for the assessment of vehicles. It assesses the average energy consumption and greenhouse gas emission of a vehicle by considering the efficiency of the vehicle's engine and the efficiency of the fuel production.

## 2 Introduction

- Reduction of fossil fuel use, due to broad range of possible hydrogen sources.
- Decrease of greenhouse gases and air pollutants.
- Increase of energy efficiency by using fuel cell technology.
- Independence on oil/gas from politically unstable countries (enhanced energy security).
- Suitable for a wide range of mass-market applications (transport sector, portable and stationary devices).
- Complements electrical power as a second energy hub with much better storage capacity.

Opinions on the role of hydrogen in the future are controversial; however, there is no doubt that tremendous barriers have to be overcome to move towards a hydrogen economy. A summary of the key hurdles and possible solutions is given in Table 2.1. Huge investments and developments in the production, storage and distribution of hydrogen, as well as in fuel cell technology, are necessary and views on whether this is achievable currently diverge. Furthermore there are many different technology options like biofuels, Fischer-Tropsch synfuels, hybrids, battery-electric vehicles, etc. that could play a more or less important role in the future. [16].

Big oil companies like Exxon and BP doubt the rise of hydrogen over the upcoming decades (possibly, of course, because of their own interests in maintaining oil demand as long as possible). They suppose that a big share of vehicles will be driven by hybrid technology and that petroleum-based products, accompanied by an increasing share of biofuels, will remain the primary fuels to cover the increasing demand for energy in the transport sector (45% more consumption in 2040 [12]). They believe that increase of efficiency of current drive systems, together with hybridisation is the best approach to meet the future consumption [12, 11].

The IEA, on the other hand, assumes that H<sub>2</sub> is likely to gain significant market shares over the upcoming decades if the costs of production, distribution and end-use fall significantly, and if effective policies are put in place to increase energy efficiency, weaken CO<sub>2</sub> emissions and improve energy security. To meet such requirements, the H<sub>2</sub> use in fuel cells for energy applications could grow, starting from 2020, to reach about 22 EJ in 2050. More than half of that hydrogen could be consumed in the transport sector, providing fuel to one-third of all cars worldwide [13].

## 2 Introduction

Hydrogen infrastructure elements	Key hurdles
<p><b>Production</b> - Hydrogen could be centrally produced in large refineries, energy complexes, or at renewable or nuclear power facilities, and locally produced in power parks, fuel stations, communities, rural areas, and on-site at customers premises. Thermal, electric and photolytic processes could use fossil fuels, biomass, or water as feedstock and release little or no CO<sub>2</sub> into the atmosphere.</p> <p><b>Delivery</b> - A national supply network would evolve over time to accommodate both centralized and distributed production facilities. Pipelines could be used to deliver hydrogen to high-demand areas. Trucks and other means could distribute hydrogen carriers to rural and other lower-demand areas.</p> <p><b>Storage</b> - A selection of relatively lightweight, low-cost, and high capacity (low weight and volume) hydrogen storage devices would be available in a variety of sizes to meet different energy needs.</p> <p><b>Conversion</b> - Fuel cells produced in high volumes would be cost-competitive, durable, and reliable and provide clear advantages in energy efficiency and emissions.</p> <p><b>Technology Validation</b> - Hydrogen could be available for every end-use energy need in the economy, including transportation, central and distributed electric power, portable power, and combined heat and power for buildings and industrial processes.</p> <p><b>Safety, Codes and Standards</b> - Model building codes that reference comprehensive equipment standards of hydrogen and fuel cell technologies for commercial and residential applications would be available for adoption by local jurisdiction.</p> <p><b>Education</b> - Businesses, government agencies, and the public may choose to use hydrogen safely and conveniently power their vehicles, provide electricity and thermal energy to their factories, offices, and homes, and run portable electronic devices. Students in a variety of disciplines would be engaged in the development, advancement, and use of hydrogen and fuel cell technologies.</p>	<p>Low cost hydrogen production techniques, low cost and environmentally sound carbon capture and sequestration technologies, advanced hydrogen production techniques from fossil, renewable and nuclear resources.</p> <p>Lower-cost hydrogen transport technology, appropriate uniform codes and standards, right-of-way for new delivery systems, high investment risk of developing hydrogen delivery infrastructure.</p> <p>Low cost, high capacity, lightweight, and low-volume hydrogen storage systems.</p> <p>Low cost, durable, and reliable fuel cells that can be mass produced.</p> <p>Successful field tests and demonstrations of integrated systems that meet customer requirements, supportive public policies to stimulate infrastructure and market readiness.</p> <p>Fuel gas code that includes hydrogen, uniform safety standards for certification of fuel cell vehicles, stationary power facilities, and portable devices.</p> <p>Widespread understanding of, and confidence in, the safe use of hydrogen as an energy carrier, access to accurate, objective information about hydrogen and fuel cell technologies, education and training for emergency responders and code officials.</p>

**Table 2.1** Hydrogen energy system infrastructure elements and key hurdles [16].

## 2 Introduction

The U.S. Department of Energy, which supervises the so-called *Fuel Cell Technology Program, FCTP*, established by the U.S. government in 2004, assumes that portable, stationary and transportation fuel cell systems driven by hydrogen will be validated between 2015 and 2020. Together with infrastructural investments, based on governmental policies, the initial market penetration will occur within this period. Between 2020 and 2040 markets and infrastructure will expand and H<sub>2</sub> power and transport systems will be commercially available. By 2040 the markets and infrastructure will be fully developed and available in all regions of the U.S. [16].

The *European Hydrogen & Fuel Cell Technology Platform, EHFP*, supported by the European Commission as well as multiple industrial companies and research institutions, initialized in 2008, reckons that the market penetration of hydrogen and fuel cells will occur around 2030 via early niche markets and that by 2050, hydrogen will cover 50% of the global demand for transport fuels [17].

The IEA, the FCTP and the EHFP agree that there won't be a single solution to cover future energy needs. Besides hydrogen, electrical energy and biofuels will play important roles in the following decades. The U.S. Department of Energy and the EHFP have released comprehensive plans on how to meet the requirements pointed out by the IEA [16, 17]. The U.S. Department of Energy has acquired more than 1 billion dollars to fund dedicated research projects since 2004 [18]. The budgets of FCTP and EHFP for 2012, respectively, reached \$100 million [19] and Euro 150 million [20], implying that there are some serious intentions to move towards a hydrogen future.

## 2.2 An overview of hydrogen production

This section gives an overview on the different pathways to producing hydrogen. Both fossil and renewable sources are considered. At the end of the section the current and prospective costs of producing hydrogen from the major technologies are compared.

### 2.2.1 Hydrogen from fossil fuels

As mentioned in section 2.1.2, nearly all of the hydrogen currently produced, comes from fossil fuels. Natural gas reforming contributed 48% of global hydrogen production, and is thus the most popular technology, followed by coal gasification (18%) and water electrolysis (4%). An additional 30% arises as a side product of oil reforming in refineries [13].

## 2 Introduction

### 2.2.1.1 Natural gas reforming

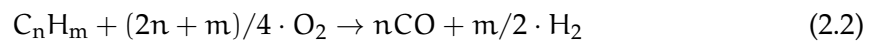
Three different technologies, namely steam methane reforming (SMR), partial oxidation (PO) and autothermal reforming (ATR), are used to convert natural gas into a hydrogen. SMR is the most common of these techniques [13].

**Steam methane reforming, SMR** During SMR the hydrocarbons present in natural gas are mainly converted via the endothermic reforming reactions in which  $\text{CH}_4$  and water are converted to CO and  $\text{H}_2$  (Equation 2.1). This happens at temperatures between 700 and 900 °C and pressures of about 30 bar in the presence of metal-based catalysts (nickel):



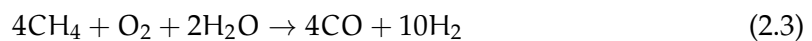
During SMR other reactions like dry reforming reactions and the water-gas shift reaction take place (see Table 2.2). As the net reaction is endothermic, a part of the natural gas is burned to supply thermal energy. The product gas, whose composition depends on process parameters like temperature, pressure, and the amount of steam added consists of up to 20% carbon monoxide, which is removed by taking advantage of the water-gas shift reaction to enhance the hydrogen yield. A pressure swing adsorption (PSA) is also performed to obtain the desired gas qualities. A more detailed description of both purification processes can be found in Section 2.3.2 [21].

**Partial oxidation, PO** In partial oxidation PO process the hydrocarbons present in natural gas are converted, together with a sub-stoichiometric amount of oxygen, to  $\text{H}_2$  and CO (Equation 2.2).



The obtained gas is processed similarly to the products from SMR. The advantage of the PO process over the SMR process is the direct heat supply [21], through the compustion of the introduced natural gas to some degree.

**Autothermal reforming, ATR** The ATR process is a combination of the SMR and PO processes, as steam and oxygen are introduced into the same reactor (Equation 2.3).

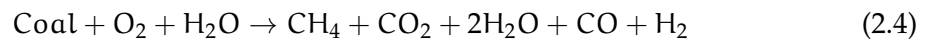


This technology was invented in order to combine the strengths of both, the SMR (high hydrogen yield) and PO (direct heat supply) processes [21].

## 2 Introduction

### 2.2.1.2 Coal gasification

During the gasification process, the coal is oxidized by oxygen and steam at elevated temperatures and a product gas mixture composed mainly of CO<sub>2</sub>, CO, H<sub>2</sub>O, CH<sub>4</sub> and H<sub>2</sub> is produced (Equation 2.4). The gaseous species produced react further in secondary reactions, in particular the water-gas shift and reforming reactions (Table 2.2, equations (viii) and (vi)). In order to increase the hydrogen yield, water-gas shift reactors are connected, and more hydrogen is produced by additional reactions with water vapour [13].



Different process setups have been developed. The main setups can be characterized as the *entrained gasifier* (General Electric former Texaco, Koppers-Totzek), the *fluidized bed gasifier* (Winkler) and the *fixed bed gasifier* (Lurgi).

### 2.2.1.3 Electrolysis

Though electrolysis produces hydrogen from water, it is considered a technique for hydrogen production from fossil fuels, because the electrical energy used to achieve separation is mostly produced from fossil fuels.

When an electrical potential is applied between two electrodes submerged in water, the following reactions take place at the cathode (Equation 2.5) and anode (Equation 2.6):



The product gas streams are then collected separately. Water is cleaned from the hydrogen-containing stream in order to obtain a hydrogen-rich gas product. Besides alkaline electrolysis technologies, membranes are also used. These systems work like reverse fuel cells, splitting water into hydrogen and oxygen. Only polymer electrolyte membrane fuel cells (PEMFC) are commercially available. Other modifications, such as solid oxide fuel cells (SOFC), need more research [21].

### 2.2.1.4 Thermal water splitting

The same considerations apply for thermal water splitting as for electrolysis. Water is the basic material from which hydrogen is derived, but the thermal energy used to achieve the separation is mostly obtained from fossil energy, and thus it is listed in this section. Heat from solar sources (Photocatalytic water splitting) could eventually be used, but

## 2 Introduction

much more effort is needed to make this technique competitive.

At temperatures above 2500 °C, water splits into its components. This process is also known as thermolysis. The high temperatures required place high demands on the materials used in the process. Furthermore, the process requires low-cost, high-temperature heat from nuclear or solar sources. Chemical processes such as sulphur-iodine (S-I) or bromine-calcium (Br-Ca) cycles could reduce the required temperatures, but much more effort is needed to make these processes competitive [13].

### 2.2.2 Hydrogen from biomass

Biomass is the only direct source of renewable hydrogen that can currently be used, without major technology breakthroughs. Current techniques can be classified as thermochemical or biological in nature. Methods in the former class, especially biomass gasification, are technologically much more advanced, and more promising. The wide variety of products obtainable from biomass (biofuels, syngas, etc.) could help to accelerate the market uptake of these processes [2].

#### 2.2.2.1 Thermo-chemical processes

**Pyrolysis** Pyrolysis is the conversion of biomass into a secondary energy carrier at temperatures above 200 °C in the absence of oxygen. Depending on the reaction kinetics a variety of products, ranging from solids to liquids to gases can be obtained. Solids are formed at low temperatures (< 450 °C) and heating rates, whereas higher temperatures (450 - 600 °C), high reaction rates and short residence times (*flash pyrolysis*) favour liquid products (pyrolysis gasoline). High temperatures (> 800 °C) and heating rates combined with long residence times lead to gaseous products; under these conditions, the term *gasification* should be used instead of *pyrolysis*, despite that no additional oxygen source is added. The reactions taking place under these conditions, are secondary reactions among the pyrolysis products evolved at lower temperatures, and are considered as gasification reactions; a more detailed description of the mechanism can be found in Section 2.3 [22]. The process at high temperatures is the favoured mechanism for hydrogen production, because it produces a gaseous mixture of H<sub>2</sub>, CH<sub>4</sub>, CO and CO<sub>2</sub> is obtained, that can be further processed via steam-reforming and water-gas-shift reactors to enhance the hydrogen yield. Moreover, hydrogen can also be obtained from oily pyrolysis products by catalytic steam reforming [2].

**Gasification** Biomass gasification is a promising method of producing hydrogen directly from renewable sources, and it is the most mature of hydrogen-from-biomass techniques. Biomass gasification is the transformation of biomass into a gaseous product at

## 2 Introduction

temperatures of about 800 °C in the presence of a gasification agent (weak oxidant). The gases can then be further processed to obtain pure hydrogen. A detailed description of biomass gasification can be found in Section 2.3, which is dedicated to the gasification process.

**Aqueous phase reforming APR** Aqueous phase reforming is one of the most recent methods of producing hydrogen from biomass. It is based on the conversion of oxygenated hydrocarbons ( $C_xH_yO_z$ ), like methanol, ethylene glycol or glucose, in the aqueous phase and over an appropriate heterogeneous catalyst (Pt, Ni, etc.) at approximately 200 °C and under 20-25 bar pressure (Equation 2.7).



Carbohydrates can be found in wastewater from biomass processing (beer brewery waste water, sugar processing), from aqueous carbohydrates extracted by steam-aqueous fractionation of lower-valued hemicellulose from biomass and other sources. APR is promising because it allows hydrogen with low CO content to be produced. This is due to the operating conditions (temperature, pressure), which favour the water-gas shift reaction, minimize undesired decomposition reactions and facilitate effective purification using pressure-swing adsorption or membrane technologies [23].

### 2.2.2.2 Biological processes

Fermentation processes may be promising as hydrogen-production methods for future commercial use and are thus the only methods considered here. Other techniques such as photolysis, in which hydrogen is produced using photosynthetic microalgae to convert energy into hydrogen, as well as biological water-gas-shift reactions, that take advantage of photoheterotrophic bacteria, are still being investigated on the laboratory scale. A more detailed description of these technologies can be found in the literature [2].

**Fermentation** In fermentation processes, a hydrogen-containing gas is produced by the decomposition of organic substrates by microorganisms under anaerobic conditions. The obtained gas contains mainly methane and carbon dioxide, but steam, hydrogen sulphides and ammoniac are also present. The conditioned gas can be introduced into a steam reforming process in order to yield a gas rich in hydrogen. Besides the classic fermentation process, dark fermentation and photofermentation are feasible process modifications. Both technologies require biomass to be pre-treated and converted into carbohydrates (glucose  $C_6H_{12}O_6$ ) [2].

## 2 Introduction

**Dark fermentation** is an anaerobic fermentation process that, in the absence of light, converts glucose into a mixture of acids, alcohols, carbon dioxide and hydrogen at temperatures between 30 and 80 °C. The hydrogen yield depends on the pH value, hydraulic retention time and partial gas pressure [21].

**Photo fermentation** on the other hand, takes advantage of the fact that special bacteria convert organic acids into hydrogen under the influence of light. The bacteria converting solar energy and biomass into hydrogen, using the nitrogenase enzyme complex [21].

### 2.2.3 Short overview of the cost of hydrogen production

This section gives a short overview of the costs of different processes for hydrogen production (stated in US\$/GJ). Only the processes considered to play a role in hydrogen production in the near future (until 2030) [13] are compared; these are steam methane reforming, coal gasification, electrolysis, biomass gasification and thermal water-splitting (sulphur-iodine cycle).

The costs of hydrogen are highly sensitive to coal, gas, biomass and electricity prices. At the moment, SMR is the cheapest hydrogen production technique available (7-16 US\$/GJ), as seen in Figure 2.2, followed by coal gasification (13-18), electrolysis (17-55) and biomass gasification (18-24). SMR seems to be on the edge in terms of efficiency (80% without considering compression), although a future reduction in cost (5-8) could be achieved by large, centralized Integrated Gasification Combined Cycle (IGCC) processes (6-9), which combine the production of syngas with the production of electricity in order to increase the process efficiency from 57% to 83%, could push coal gasification; whereas advanced materials and the introduction of membrane electrolysis techniques could enhance interest in electrolysis methods (17-23). Introducing carbon capture and storage (CCS) technologies could help all of these processes meet environmental requirements, but would bring lower efficiencies and higher costs.

Biomass gasification (currently 17-23, future 13-16.5) might not be able to compete with large-scale SMR and IGCC plants, as a limited feedstock availability would limit the profitability of large-scale biomass gasification, but could compete with small-scale SMR and electrolysis processes. Notably the sensitivity of hydrogen cost to fuel prices could make biomass gasification interesting, as receding fossil resources will sooner or later lead to an increase of energy costs [13].

## 2 Introduction

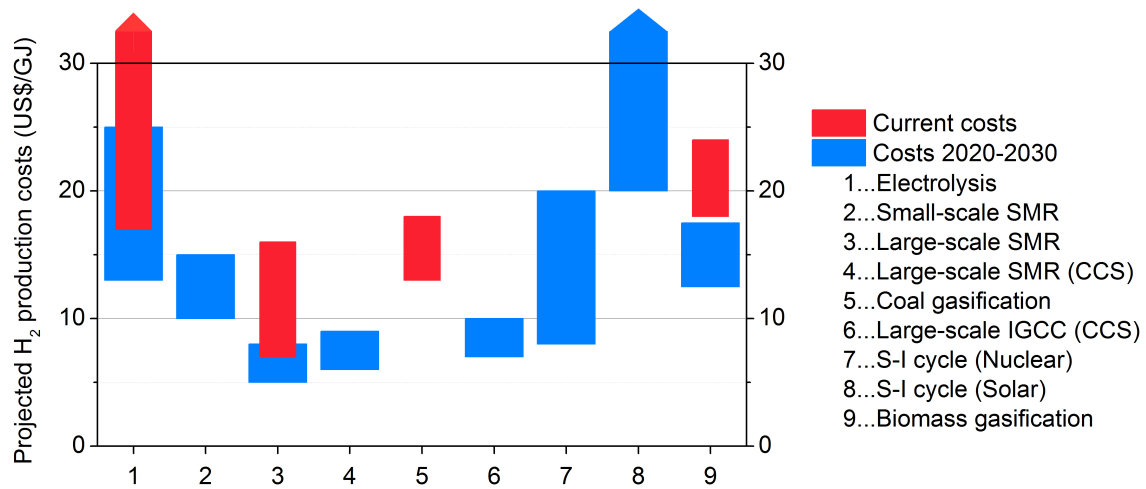


**Figure 2.2** Current and projected (2020-2030) hydrogen production costs, sensitive to technologies, dependent on assumed energy prices. Re-drawn from reference [13].

## 2.3 Hydrogen from biomass gasification

### 2.3.1 Fundamentals

Biomass gasification is the conversion of biomass (biogenic, non-fossil materials like wood, plants, organic waste, etc.) into a gas mixture containing  $H_2O$ ,  $CO$ ,  $CO_2$ ,  $CH_4$ ,  $H_2$ , light hydrocarbons, condensable tars, nitrogen and sulphur components as well as solid products (ash, char) through the reaction with a gasification agent under substoichiometric conditions. The product is a secondary energy carrier, which can be used in various applications [22].

Strictly speaking, gasification is the conversion of a solid reagent into a gaseous product only. As biomass passes through various conversion steps, namely drying, pyrolysis and gasification, before the actual product gas is obtained, it is common to speak of the technical realization of biomass gasification as an interaction of these three steps. This makes sense, because most organic material (80 - 85%) is decomposed during the pyrolysis step, which therefore is crucial for the final distribution of the product gas [22].

**Drying** At temperatures up to  $200\text{ }^\circ\text{C}$ , water present in the pores of the biomass and bound in the organic matter is released. The process of drying, also called dehydration, is endothermic, and causes almost no degradation of the organic matter [22].

**Pyrolysis** During this step, the macromolecules that make up biomass are decomposed in the absence of oxygen, as explained in Section 2.3.2. Pyrolysis starts at about  $200\text{ }^\circ\text{C}$

## 2 Introduction

and ends at about 500 °C, and converts 80 - 85% of the biomass into gaseous products. The residue consists largely of ash and fixed carbon. The process begins with the endothermic release of mainly incombustible gases like CO<sub>2</sub>, but also CH<sub>2</sub>O and C<sub>2</sub>H<sub>4</sub>O<sub>2</sub> below about 280 °C. Then combustible species like CH<sub>4</sub>, CO, H<sub>2</sub>, CH<sub>3</sub>OH, C<sub>2</sub>H<sub>4</sub>O<sub>2</sub> and CH<sub>2</sub>O<sub>2</sub> are built during exothermic reactions between 280 and 500 °C. Above these temperatures, endothermic processes yield mostly H<sub>2</sub> and CO due to the decomposition of gases released by organic matter passing through charred material. Pyrolysis occurs under oxygen-free conditions. Even if oxygen were present, it could not react with the biomass particles, because volatile species are released during this step and funnel out of the particles, preventing oxygen from reaching the reaction zone [22].

**Gasification** Gasification is the reaction of the solid residue from pyrolysis step with an additional gasification agent that is introduced into the process to form a combustible gas. Additionally, the volatile compounds produced during pyrolysis react amongst themselves and the oxidizing agent in so-called secondary reactions. These may also occur during the actual pyrolysis step itself at higher temperatures, as oxygen-containing species evolve during pyrolysis. All of these reactions occur at elevated temperatures (from about 600 °C) at substoichiometric conditions.

The present reactions are summarized in Table 2.2. Equations (i) to (v) describe the gas-solid reactions that occur during the conversion of solid biomass to gas. Equations (vi) to (ix) are the homogeneous reactions happening among the pyrolysis and gasification products, as well as between these and the gasification agent.

Reaction	Equation		$\Delta H_{298.15}^0$
Char oxidation	$C + O_2 \rightarrow CO_2$	(i)	- 395.5
Partial char oxidation	$C + 1/2O_2 \leftrightarrow CO$	(ii)	- 110.5
Heterogeneous water-gas	$C + H_2O \leftrightarrow CO + H_2$	(iii)	+ 118.5
Boudouard	$C + CO_2 \leftrightarrow 2CO$	(iv)	+ 159.9
Hydrogenating	$C + 2H_2 \leftrightarrow CH_4$	(v)	- 87.5
Water-gas shift	$CO + H_2O \leftrightarrow CO_2 + H_2$	(vi)	- 40.9
Methane reforming	$CH_4 + H_2O \leftrightarrow CO + 3H_2$	(vii)	+ 206.2
Steam reforming	$C_xH_y + xH_2O \leftrightarrow xCO + (x + 1/2y)H_2$	(viii)	+
Dry reforming	$CH_4 + CO_2 \leftrightarrow 2CO + 2H_2$	(ix)	+ 247.3

**Table 2.2** Main heterogeneous (i)-(v) and homogeneous (vi)-(ix) reactions occurring during biomass gasification.  $\Delta H_{298.15}^0$  in kJ/mol stands for the standard enthalpy of formation. (-) indicates exothermic, (+) endothermic reactions.

The pressure and temperature and gasification agent all effect the reaction equilibria and

## 2 Introduction

therefore the final product distribution. Air, steam, oxygen, or carbon dioxide or even a mixture of these, can be used as the gasification agent, which provides the oxygen atoms required for the oxidation reactions. Air may be the most economic agent, but necessarily dilutes the final product with nitrogen resulting in a product of low heating value. A detailed comparison of the various gasification agents can be found later in this section. As biomass gasification is an overall endothermic process, heat must be supplied. This can be realized by partial combustion of the biomass (autothermic process) or via heat exchanger or heat carrier (allothermic process) [22].

The variant of the gasification process can be collected into three groups: those in fixed-bed gasifiers (updraft and downdraft), fluidized-bed gasifiers (bubbling and circulating), and entrained-bed gasifiers.

**Fixed-bed gasification** In this procedure the biomass is present in a fixed bed, perused at low flow rates by a gasification agent. Depending on the relative motion between the downwards-moving biomass (due to a continuous burn-off) and the gasification agent, the system can be classified as an **updraft and downdraft gasifier** can be distinguished. Certain reaction zones in which the different conversion steps (drying, pyrolysis, gasification) occur, develop within the fixed bed. The strength of updraft gasifiers is the relatively low temperature of the product gas that leaves the reactor; this produces high efficiencies, while putting low requirements on the raw biomass. Their drawbacks are the relatively high contents of tars and water in the product gas. Downdraft gasifiers produce products with smaller amounts of impurities (mainly tars). However, the efficiency is lower, because the gas leaves the gasifier at higher temperature. Moreover, the biomass must be drier than with updraft gasifiers, and the risk of slack formation is greater [22].

**Fluidized-bed gasification** During fluidized-bed gasification a bed material (usually silica sands) is fluidized by the gasification agent and whirled around in the reactor. The biomass is then fed into the reactor where it reacts with the agent at temperatures at about 800 - 850 °C. Due to the excellent mixing of the reactants and the high surface area of the particles, short residence times and high conversion rates of the introduced feedstock can be obtained. In contrast to fixed-bed gasification no clear reaction zones are formed. The discharge of particles is, logically, higher than from fixed bed reactors and the tar content lies between the updraft and downdraft gasifiers [22].

Depending on the flow rate, fluidized bed reactors can be characterized as **bubbling fluidized-bed** reactors and **circulating fluidized-bed** reactors. To achieve high-purity

## 2 Introduction

gases, a combination of more than one reactor can be used. In bubbling fluidized beds, the flow rate is limited so that the particles remain suspended, leading to continuous reaction conditions. The discharge of particles is rather low. Circulating fluidized beds work at higher flow rates, and aim to discharge particles, which then are recycled into the reactor using cyclones. The aim of this process is to enhance the carbon conversion and its advantage is that it can achieve performances obtained in a bubbling fluidized-bed at smaller dimensions. This is associated with higher process-regulation efforts and cost, though, so profitability can only be secured at larger-scale. A drawback of all fluidized bed reactors is the high outlet temperature of the product gas, which makes heat recovery facilities necessary [22].

**Entrained bed gasifiers** In entrained bed gasifiers, finely ground biomass is blown through a reactor together with the gasifying agent. The fine particles are completely gasified within a few seconds, as the temperatures in the reaction zone lies between 1200 and 2000 °C. Due to the high temperatures, this process can be of advantage when converting materials with critical ash-melting behaviour. On the other hand it requires high-end materials to handle the elevated temperatures and big efforts in process regulation [22].

### 2.3.2 Purification processes

The product gas obtained during the actual gasification process, is a mixture whose hydrogen content is highly sensitive to method and conditions used and varies between 10 and 65% [2]. As proton exchange membranes (PEM) fuel cells, which are among the most promising fuel cells, require > 99.9% hydrogen [3], measures have to be taken to enhance the hydrogen share. This can be achieved in several ways, in particular by using downstream gas-cleaning processes, adjusting the process conditions, or using catalysts during gasification.

#### 2.3.2.1 Downstream gas cleaning

Downstream gas cleaning is a substantial step on the way from raw biomass to the desired products, regardless of whether these are biofuels, syngas or hydrogen. The removal of tars, undesired sulphur and nitrogen and chloro compounds and dust particles is crucial to yield a high-quality gas product. As a discussion of all these processes would go beyond the scope of this work, only the removal of the main species, CH<sub>4</sub>, CO and CO<sub>2</sub> is addressed. More detail can be found in the literature [22].

**CH<sub>4</sub> separation** In order to remove CH<sub>4</sub> or other hydrocarbons, steam-reforming reactors are used. These reactors are mostly applied to convert natural gas into a hydrogen-

## 2 Introduction

rich product, as discussed in Section 2.2. The gas obtained from biomass gasification and introduced into the steam reforming reactor has a different composition from the natural gas. In particular content of CO<sub>2</sub> is substantially higher, so dry-reforming reactions are favoured [21].

**CO separation** The product gas is processed in a further reactor in order to convert excess CO into H<sub>2</sub> by introducing steam into the reactor and taking advantage of the water-gas shift reaction. Whereas low temperatures favour the hydrogen production through a shift of reaction equilibrium, the reaction runs faster at higher temperatures, so the reactor is often split into two parts. First the bulk of CO is converted at temperatures of 300-500 °C in the presence of iron-based catalysts. During the second step, the gas is lead into a lower-temperature reactor, where the equilibrium shift causes further conversion of CO into H<sub>2</sub>. Between 180 and 300 °C using copper-based catalysts. In between the two reactors, the gas stream has to be cooled due to the exothermic nature of the water-gas shift reaction.

**CO<sub>2</sub> separation** CO<sub>2</sub> separation can be achieved via absorption. Physical or chemical solvents can be used. The separation via physical solvents is based on Henry's law ( $p_{ges} \cdot y_i = H_i \cdot x_i$ ), which describes the solubility of different gases in a liquid phase; this is usually higher at low temperatures and high pressures. When chemical solvents, like mono-ethanol amine (MEA) are used, in addition to the Henry absorption, chemical reactions that further enhance the CO<sub>2</sub> separation take place. In case of MEA, water reacts with CO<sub>2</sub> which then leads to further reactions of MEA and the formed species. MEA processes are conducted in packed columns at temperatures of 40-55 °C, pressures of 1-3 bar and MEA concentrations of about 30 wt.%. MEA can be almost completely regenerated, by applying steam to heat the solvent up (100 - 120 °C) the solvent and decrease its ability to dissolve CO<sub>2</sub> [21].

Another technique, which is often used as a final cleaning step, is pressure swing adsorption (PSA). CO<sub>2</sub> is adsorbed in fixed bed reactors at elevated pressures (15-35 bar) and temperatures of about 40 °C, using active carbon, alumina, zeolites, silica gel or molecular sieves as the bed material. As the adsorption capacity of the bed material decreases with the degree of loading, the impurities have to be regularly desorbed by decreasing the pressure to 0.14-1.5 bar. To accomplish a continuous process, up to 12 fixed beds are used in combination. Up to 99.999% pure hydrogen can be produced by using this technology [21].

Membranes and the separation via condensation at cryogenic temperatures are two other

## 2 Introduction

possible technologies, but both need more research before they can be applied on a large-scale. A comprehensive discussion of the different CO<sub>2</sub> capture systems can be found in reference [24].

### 2.3.2.2 Operation conditions

Besides downstream gas cleaning technologies, changing the operation conditions can change the product gas distribution and therefore the hydrogen content. Such measures are known as primary measures, and reach from the variation of temperature and pressure and the use of different gasification agents through the modification of reactor design and the choice of different feedstocks to the use of various bed materials and catalysts (see Section 2.4). It has to be considered that the studies mentioned in this section cover just a small part of the research which has been done in this context.

**Temperature** Franco et al. [25] studied the effect of different parameters on biomass gasification, gasifying softwood (pinus pinaster) and hardwood (eucalyptus globulus and holm-oak) in a bench scale fluidised bed gasifier using steam, which was indirectly heated by an electrical furnace, as the gasification agent. They found that higher temperatures (at a constant steam/biomass ratio of 0.8) favoured the formation of H<sub>2</sub>. An increase in temperature from 730 to 850 °C gave a rise in H<sub>2</sub> content of 10-20 up to 45 mol% and a decrease in all other compounds, namely CO, CO<sub>2</sub>, CH<sub>4</sub>, C<sub>n</sub>H<sub>m</sub> and tars. Higher temperatures lead to even higher H<sub>2</sub> shares in the product gas, but were associated with a decrease in process efficiency [26].

Turn at al. [27] investigated hydrogen production from sawdust in an electrically heated bench-scale fluidized-bed gasification system using oxygen, nitrogen and steam as fluidizing agents. They revealed an increase in hydrogen concentration from 31 to 45 vol% upon raising the temperature from 750 to 950 °C (at a steam-to-biomass ratio<sup>3</sup> of 1.4 and an equivalence ratio ER<sup>4</sup> of 0.18). The increase in hydrogen, came along with slight decreases in the concentration of carbon dioxide, methane and higher hydrocarbons (due to more favourable conditions for thermal cracking). The level of carbon monoxide remained rather constant over the investigated temperature range.

Another survey, conducted by Pfeifer et al. [26], addressed the influence of various operation conditions on the steam gasification in a 100-kW dual-fluidised-bed gasifier. In order to achieve the temperatures necessary for the gasification reactions, the systems

---

<sup>3</sup>the steam-to-biomass ratio is defined as the total of the mass of steam + the mass of moisture content of the used biomass, relative to the mass of the dry biomass.

<sup>4</sup>The equivalence ratio ER, which is also known as the Lambda value  $\lambda$  is defined as the actual mass of oxygen participating in an oxidation process, relative to the stoichiometric mass of oxygen

## 2 Introduction

consisted of two zones: (i) the gasification zone, in which the biomass was converted into a gaseous product and charcoal using steam as the gasification agent, and (ii) the combustion zone (riser), in which the char coal from the gasification zone was fluidized with air and combusted at temperature of about 920 °C. The bed material circulated between the two zones, transferring the the heat produced from combustion to the gasification zone. The work demonstrated, that higher temperatures favoured hydrogen yield (from about 34 vol% at 750 °C to more than 40 vol% at 850 °C). The share of CO<sub>2</sub> and CH<sub>4</sub> in the product gas decreased with rising temperatures as did the tar content. CO<sub>2</sub> increased slightly. Pfeifer et al. proposed that although higher temperatures lead to higher hydrogen yields, an optimum balance between temperature and H<sub>2</sub>-yield was required, as the efficiency of a gasification process decreases with higher reaction temperatures.

**Gasification agent and steam-to-biomass ratio** In a gasification process, the gasification agent is basically responsible for the oxidation of the solid residues from the pyrolysis step as well as for fluidizing the bed material and the biomass. Gasification agents range from air and oxygen through CO<sub>2</sub> to steam and influence the product gas distribution as well as the process setup substantially. Air is the cheapest gasification agent, however, the product gas obtained from air-gasification is diluted with nitrogen and therefore of low energy content [22]. Oxygen facilitates the partial combustion of biomass to achieve the reaction temperatures, but requires an expensive oxygen plant [25]. Steam has been found to be the most suitable gasification agent, as it increases H<sub>2</sub> output via the water-gas shift and steam-reforming reactions [28, 29].

Gil et al. [29] examined the effect of different gasification agents, namely air, a steam-oxygen mixture and pure steam, on the product distribution of a bench-scale bubbling fluidized bed. Pure steam gave the highest hydrogen yield (53-54 vol%) among the three different gasification agents (cf. air 8-10 vol%; steam-O<sub>2</sub> 25-30 vol%), at 750 to 780 °C and a steam-to-biomass ratio of 0.9. It also led to the product gas with the highest lower heating value (LHV), namely 13.3 MJ/nm<sup>3</sup> (dry) and, as a drawback, the highest tar content (30-80 g/nm<sup>3</sup>).

The influence of the steam-to-biomass ratio has been investigated by different research groups [25, 26, 27, 29]. All of them, despite using different gasification setups and conditions, agree that an increase in the steam-to-biomass ratio leads to a raised hydrogen yield. Pfeifer et al. [26] and Franco et al. [25] furthermore confirmed a slight increase in CO<sub>2</sub> formation and decreases in CO, CH<sub>4</sub>, and tar formation, as well as in process efficiency, at higher steam-to-biomass ratios.

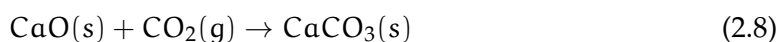
## 2 Introduction

**Equivalence ratio, ER** Gasification processes work at substoichiometric conditions compared to complete combustion. A coefficient used to describe these conditions is the equivalence ratio (also known as Lambda,  $\lambda$ ), the ratio between the actual mass of air divided by the stoichiometric mass of air needed to completely oxidize a material. Turn et al. [27] and Gil et al. [29] investigated the influence of the equivalence ratio on the product distribution of gasification. Turn et al. showed that decreasing ER (from 0.37 to 0.00) caused an increase in hydrogen share (27.6 to 46.8 vol%, dry), whereas carbon dioxide exhibited an opposing trend, decreasing from 47 to 22 vol%. This was confirmed by Gil et al., who increased the hydrogen yield (dry) during steam gasification from  $\leq 20$  vol% at ER=0.50 to close to 50 vol% at ER=0.00.

**Reactor design and feedstock used** Different feedstocks varying in chemical (cellulose, hemicellulose, lignin) and elemental composition and in content of moisture, volatiles and minerals give different product compositions in gasification processes. Besides that, reactor design is crucial to the gasification process. Reactor dimensions, gas flow rate, type of gas distributor and biomass feeding point are only some of the factors that influence the degree of contact between the biomass and gasification agent, the temperature and the gas residence time. An overview on the influence of the reactor design and feedstock can be found in the literature [3].

**CO<sub>2</sub> capture** The hydrogen share in the product gas of a gasification process can be enhanced by in situ CO<sub>2</sub> capture, which causes shifts in the equilibria of the reforming reactions and the water-gas shift reaction. Theoretically speaking, various CO<sub>2</sub> capture processes, including the downstream processes discussed in this work (see Section 2.3.2.1), or the use of metal oxides could be used for this purpose. The harsh atmosphere present in a gasification reactor excludes most of these processes, though, as they require specific process conditions.

A suitable CO<sub>2</sub> sorbent may be CaO, since it is low cost, abundant and capable of working at temperatures of 450 - 750 °C [3]. Using CaO as the sorbent, CO<sub>2</sub> is captured as CaCO<sub>3</sub>, according to the following exothermic reaction:



Thus this CO<sub>2</sub> adsorption shifts the reforming and water-gas shift equilibria and further enhances the process due to the lower reaction temperatures [30].

Different experimental investigations have been made by, for example Lin et al. [31] (HyPr-RING process), Pfeifer et al. [30] (Adsorption Enhanced Reforming AER process)

## 2 Introduction

or Hanaoka et al. [32]. The former investigated the gasification of a mixture of coal and CaO powders with steam in a continuous-flow reactor at 650 °C and elevated pressures (1.0 - 6.0 MPa). The process yielded a gas mixture of 76 vol% H<sub>2</sub>, 17 vol% CH<sub>4</sub> and 2 vol% CO<sub>2</sub> at a pressure of 5.0 MPa.

Pfeifer et al. [30] and Hanaoka et al. [32] both used biomass fuels instead of coal. Hanaoka et al. investigated the steam gasification of woody biomass (Japanese oak) with Ca(OH)<sub>2</sub> powder in a batch reactor, varying the pressure and the sorbent loading at constant temperature (600 °C). They revealed an increase of the hydrogen yield of 50 to 80.7 vol%, when the gasification was coupled with CO<sub>2</sub> capture (mol Ca/mole C = 2, p = 6 atm). A pressure increase from 1 to 10 atm slightly increased the hydrogen yield. Pressures above 10 atm caused a dramatic drop in hydrogen concentration in the product gas.

Pfeifer et al. [30] reported hydrogen yields of 75 vol% in the product gas of a dual-fluidized-steam gasification process (100 kWh), using olivine doped with Cao as the bed material and working at atmospheric conditions. The process was split into two separate reaction zones; (i) a gasification zone, where the actual gasification and the CO<sub>2</sub> sorption took place (Equation 2.8) and (ii) a combustion zone, where the charcoal obtained during the gasification process as burned in air and the sorbent is regenerated. The bed material circulated between the two zones, providing the heat required for the gasification process.

## 2.4 Catalysts in biomass gasification processes

### 2.4.1 Fundamentals

Reducing the tar content in the product gas obtained from biomass gasification is the most prominent reason for the use of catalysts. Plugging in colder parts of a gasification facility or plants makes the removal of tars crucial. Moreover, tars contain hydrogen atoms that can yield more H<sub>2</sub>. Catalytic cracking is more promising than other possible cleaning measures, like thermal cracking, mechanical cleaning or cracking through a change in operation conditions [33], because (i) the tars are destroyed the reactor itself (e.g this is a primary measure), with no need for additional cleaning facilities or extra cleaning effort, and (ii) the conversion contributes to the heating value of the product gas, increasing the overall efficiency of the biomass conversion by up to 10% [34]. Comprehensive discussions on catalysts for the purpose of tar elimination in biomass gasification processes can be found in the literature [33, 34, 35]. Table 2.3 gives an overview of the available catalysts and compared their strengths and weaknesses.

## 2 Introduction

Catalyst	Advantages	Disadvantages
Calcined rocks (dolomite, limestone)	Inexpensive and abundant, tar conversion of 95%	Fragile material and quickly eroded from fluidized beds
Olivine	Inexpensive, high attrition resistance	Lower catalytic activity than dolomite
Clay minerals	Inexpensive and abundant	Lower catalytic activity than dolomite, do not support high T (800-850 °C needed for tar elim- ination)
Iron ores	Inexpensive and abundant	Rapidly deactivated in the ab- sence of hydrogen, lower cat- alytic activity than dolomite
Char	Inexpensive, natural produc- tion inside the gasifier, high tar conversion, comparable with dolomite	Consumption because of gasifi- cation reactions
FCC (zeolites)	Well-investigated, high tar con- version	Rapid deactivation by coke
Alkali-metal-based (Na, Li, Ka)	Natural production in the gasi- fier	Particle agglomeration at high temperatures, lower catalytic ac- tivity than dolomite
Activated alumina	High tar conversion comparable with dolomite	Rapid deactivation by coke
Transition-metal-based (Ni, Pt)	Able to attain complete tar elim- ination at about 900 °C, increase yield of CO <sub>2</sub> and H <sub>2</sub> , Ni-based catalysts are 8-10 times more ac- tive than dolomite	Rapid deactivation because of sulphur and high tar content in the feed, relatively expensive

**Table 2.3** Summary of catalysts used as primary measures in biomass gasification processes comparing their advantages and disadvantages [35].

## 2 Introduction

The catalytic decomposition of tars involves mainly reforming reactions that take place at the catalyst surface [34] and lead to a product gases with enhanced H<sub>2</sub> and CO content.

In order to increase H<sub>2</sub> yield, both the water-gas shift reaction and reforming reactions must occur. As the tar-cracking and steam reforming reactions are typically endothermic and therefore favoured at high reaction temperatures (> 800 °C), but the water-gas shift reaction is exothermic, a trade-off in the gasification temperature has to be made. Appropriate catalysts facilitate the decomposition of tars and promote steam-reforming reactions at temperatures more suitable for the water-gas shift reaction, producing a product that contains mainly H<sub>2</sub> and CO<sub>2</sub> [6].

Such catalysts are commonly known as steam-reforming catalysts, as their main field of application is the SMR process (see Section 2.2) [35], but they have been applied in various technologies to convert a wide range of feedstocks, including in biomass gasification [5, 26, 36, 37, 6, 7].

### 2.4.2 Catalysts to enhance the H<sub>2</sub> yield during biomass gasification

Most of the catalysts used for tar elimination during biomass gasification (see Table 2.3) accelerate steam- and dry-reforming reactions as well as the water-gas shift reaction to some degree [34, 35]. The biggest share of the research on catalysts for biomass gasification have focused on alkaline earth metal oxides like limestone and dolomite, on olivine and on Ni-catalysts. More recently, some research on cobalt catalysts has been reported as well [38]. This section gives only a short overview of the catalysts that have been used to enhance the hydrogen yield during biomass gasification.

**Non metallic oxides** Non-metallic oxides are naturally occurring and relatively inexpensive materials. They show good performance in tar elimination and are the most popular catalysts for this purpose, but produce a less-distinct increase in hydrogen in the product gas, than the other catalysts mentioned in this section . They are often used as guard beds for expensive catalysts [35].

Pfeifer et al. [36], for example, investigated the impact of different bed materials, among others olivine, Fe-olivine and Ni-olivine, on the product gas distribution in dual-fluidised-bed biomass gasification (100 kW pilot plant). They showed that the incorporation of Ni onto olivine enhanced the hydrogen yield from about 39 to 44 vol% (dry) and reduced the tar content from about 3.5 to 1 g/nm<sup>3</sup> (dry). Fe-doped olivine exhibited the smallest share of hydrogen in the product gas together with the highest amount of CO<sub>2</sub> and the lowest amount of CO, confirming that Ni-olivine was the best catalyst to enhance the hy-

## 2 Introduction

drogen production. In the same work they compared silica-sand, olivine and limestone as the bed materials. Limestone showed the best performance, reaching hydrogen contents of 48-51 vol% (dry) and tar contents of 0.5-2 g/nm<sup>3</sup> (dry); however, it was subject to attrition.

**Nickel catalysts** Nickel has been found the best catalyst for the purpose of hydrogen production. Like every group VIII metal (Pt, Ru, Ir, Rh, etc.), it shows excellent reforming behaviour. Due to its abundance and low cost, it is the most widely used catalyst in industry, and is the active element in nearly every commercial reforming catalyst [37, 39]. Using nickel at >740 °C generally increases hydrogen and carbon monoxide content in the product gas, and eliminates or reduces tars and methane [34]. Nickel has been identified as one of the best metals for tar elimination, because it catalyzes C-C, O-H and C-H bond cleavages as well as the water-gas shift reaction [23]. According to El-Rub et al. [35], nickel-based catalysts are 8-10 times more active than calcined dolomites under the same operating conditions.

The problem with several types of catalysts but especially with Ni catalysts, is that deactivation occurs in the reactors due to (i) attrition through mechanical forces, (ii) loss of the surface area through sintering at high temperatures, (iii) coking (fouling), which is the blockage of catalyst surface area by coke and (iv) poisoning, which is the strong chemisorption of H<sub>2</sub>S and other compounds onto the catalyst active sites. Some of these problems can be addressed by choosing a suitable gasification setup (fluidized bed, dual fluidized bed, etc.). Another problem of Ni-containing catalysts is that they are more expensive than naturally occurring minerals [35].

**Cobalt catalysts** Cobalt has been reported as an effective catalyst in various applications, showing good activity for C-C bond rupture, tar decomposition, steam reforming and the water-gas shift reactions [5]. These abilities, together with the coking issues of Ni-catalysts, increased the interest in Co catalysts [38]. Co-containing catalysts are more active in catalysing the water-gas shift reaction than Ni-containing species. The use of cobalt together with nickel as bimetallic catalyst has also been reported; these show higher catalytic activity and higher resistance against carbon deposition than Ni catalysts [5].

Zhao et al. studied the hydrogen yield during cellulose decomposition on the lab scale using Ni, Co and Ni-Co catalysts, on different support materials [5, 7, 6]. They revealed a significant rise in hydrogen yield when any catalyst was used, but the bimetallic Ni-Co catalyst exhibited the most significant enhancement in catalysis of cracking, reforming

## 2 Introduction

and water-gas shift reaction and gave high coke resistance.

### 2.4.3 Catalyst support materials

The Ni and Ni-Co catalysts prepared by Pfeifer et al. and Zhao et al., discussed in the previous section of this work, both used substrates to support the active material. This is, aside from the combination with other materials, another measure to improve the catalysts' performance and overcome the aforementioned issues. Support materials must offer strength against the harsh conditions inside a reactor, prevent attrition and sintering and improve the performance and durability of a catalyst. They also interact with the active metal sites, changing the properties of the catalyst and this can further impact the catalyst behaviour. Promoters like Mg or K can also be added to stabilize the active metal crystallite size or neutralize the support surface area acidity thus decreasing coke deposition [35]. Various materials have been used as support materials. In particular inexpensive calcined rocks (MgO or CaO), activated alumina ( $\text{Al}_2\text{O}_3$ ), aluminium mixed-metal oxides ( $\text{MgAl}_2\text{O}_3$ ), zirconia ( $\text{ZrO}_2$ ), silicon carbide (SiC) and silica ( $\text{SiO}_2$ ) are common substrates [7].

Additionally, microporous and mesoporous<sup>5</sup> molecular sieves have attracted increasing attention as catalyst supports over the last 15 years. Tailored to the specific needs of an application, they show several advantages over other support materials [41]:

- Very high surface areas ( $> 1000 \text{ m}^2/\text{g}$  compared to  $<200 \text{ m}^2/\text{g}$  for the standard support materials), large pore volume and adsorption capacity allowing long-range interaction with atoms, ions and molecules entering the pore framework.
- Uniform poresize distribution in microporous and/or mesoporous range, separating certain molecules from others.
- Controllable surface chemistry.
- Even distribution of active sites on their surface area promoting catalysis.

Among these synthetic materials, **zeolites**, which are microporous aluminosilicates, are the most widely used catalyst supports in industry. In addition to the advantages listed above, they highly resist to heat, steam and chemical attacks, all of which present in processes like biomass gasification. The drawback of zeolites is that their pores are relatively small (0.8-1.2 nm). To convert relatively large molecules, like tars, bigger pores are

---

<sup>5</sup>According to the International Union of Pure and Applied Chemistry (IUPAC) porous materials are classified into three groups, (i) microporous materials with pore diameters  $< 2 \text{ nm}$ , (ii) mesoporous materials with pore diameters between 2 and 50 nm, and (iii) macroporous materials with pore diameters  $> 50 \text{ nm}$  [40].

## 2 Introduction

required, as they allow the molecules to enter the support framework and interact with the active sites deposited on its surface area [42].

Mesoporous silicates and aluminosilicates, known as **M41S materials** are the second big group of molecular sieves and are capable of gathering tars, as their pore diameters range from 1.5 to 10 nm. This, combined with surface areas of more than 1000 m<sup>2</sup>/g, well-ordered pore structures and narrow pore-size distributions make them suitable support materials for the conversion of tars and other big molecules. MCM-41, SBA-15 and KIT-6, which are all mesoporous forms of silica (SiO<sub>2</sub>), are some of the most popular kinds of M41S materials, which have been applied as catalyst supports in various applications [5, 6, 7, 42].

Zhao et al [7], for example, used  $\gamma$ -Al<sub>2</sub>O<sub>3</sub> and MCM-41 as support materials for Ni catalysts in cellulose pyrolysis. They found that the use of highly ordered, mesoporous structure of MCM-41 (surface area = 965 m<sup>2</sup>/g) and a Ni content of 5 wt.% yielded more than twice the H<sub>2</sub> that was obtained using  $\gamma$ -Al<sub>2</sub>O<sub>3</sub> (surface area = 122 m<sup>2</sup>/g) and the nickel loading.

Another group of materials, the **non oxide ceramics**, such as silicon carbides and silicon nitrides, can be synthesized with ordered structure and large surface area and have recently attracted attention. This is due to their unique mechanical and functional characteristics, like excellent mechanical and hydrothermal stabilities and chemical inertness [4]. Oxide materials like SBA-15 admittedly show high mechanical and thermal stability but exposure to steam at high temperatures leads their pore structure to collapse, causing a significant decrease of surface area and the number of active sites [43, 44]. As steam gasification is the most promising type of biomass gasification, catalysts must be hydrothermally stable. Mesoporous non-oxide ceramics are therefore promising support materials.

## 3 Experimental

This chapter addresses the synthesis, characterization and testing the SiC-supported catalyst and its precursor, SBA-15<sup>1</sup>. The materials were chosen, following studies conducted at the Laboratory of Sustainable Technology at The University of Sydney, where a well-ordered mesoporous-silica-(SBA-15)-supported Ni-Co catalyst with a very high surface area was developed. This catalyst performed remarkably well in the production of hydrogen during the pyrolysis and gasification of cellulose [5]. The same group synthesized a mesoporous silicon carbide (SiC) material, that was used in a carbon dioxide sorbent [45]. This material did not have the high surface area and ordered structure of the silica support, but is considered hydrothermally much more stable than SBA-15 [43, 44, 4], which is essential for the use in the harsh environment of steam gasification. Based on these investigations, the idea arose, to examine the behaviour of SiC as a catalyst support in biomass gasification.

### 3.1 Synthesis of catalyst

#### 3.1.1 Synthesis of SBA-15

SBA-15 was synthesized using a liquid crystal templating sol-gel process, respectively, published by Zhao et al. [46], and was used both as a catalyst support and as a template for the synthesis of mesoporous SiC. The liquid crystal templating (LCT) process, proposed by Beck et al. [47] used Pluronic P123 (PEO<sub>20</sub>PPO<sub>70</sub>PEO<sub>20</sub>, PEO = poly(ethylene oxide), PPO = poly(propylene oxide)) as the copolymer surfactant and tetraethylorthosilicate (TEOS, (C<sub>8</sub>H<sub>20</sub>O<sub>4</sub>Si) as the silica source.

##### 3.1.1.1 Method

**Liquid crystal templating LCT** During the LCT process, a copolymer surfactant builds surfactant micelles in aqueous solutions. Subsequently, micellar rods are built and, after adding a silica source a hexagonal array of micellar rods surrounded by a framework of silica is produced. In the last step, the template is removed by calcination in air. The exact

---

<sup>1</sup>SBA-15 is a mesoporous silica material, which was invented at the University of California, Santa Barbara. The name, which stands for Santa Barbara Amorphous type material number 15, is dedicated to the material's location of origin.

### 3 Experimental

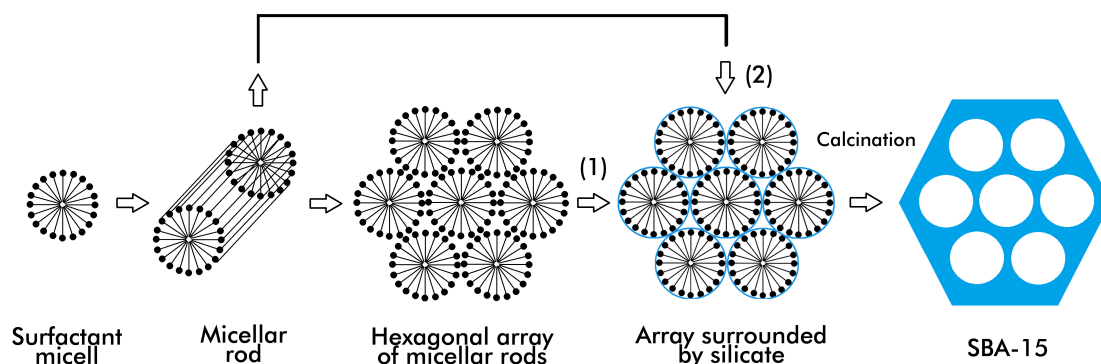


**Figure 3.1** Possible mechanistic pathways of the formation of SBA-15: (1) liquid crystal phase initiated and (2) silicate anion initiated. Re-drawn from reference [47].

mechanism of organizing the hexagonal array hasn't been resolved yet, as it is highly sensitive to solution conditions (concentration, temperature, etc.) as well as to the silica source which is a complex system of liquid crystalline phases. It is uncertain whether the organization occurs independently of the silicate crystallization, or whether silicate anions, present in solution, after the silica source is added direct the formation of the micellar arrays. In both proposed mechanisms a liquid crystal template is implicated. The LCT process considering both possible pathways of the hexagonal array formation is shown in Figure 3.1 [47, 48].

**Sol-gel process** The silica, polymerizing around the surfactant aggregates, is obtained via the so-called sol-gel process. The silica source is hydrolysed to orthosilicic acid,  $\text{H}_4\text{SiO}_4$ , and ethanol which is then decomposed to silicon dioxide through dehydration. The first colloids to precipitate act as the precursor for an integrated network (or gel) of either discrete particles or network polymers depending on the reaction time (aging). The overall reaction is shown in Equation 3.1, for the case of TEOS as the silica source. As TEOS is insoluble in water, ethanol is usually used a co-solvent. Acidic or alkaline solutions can be used, and both, catalyse the reactions [49].



**Literature** Zhao et al. [46] conducted comprehensive studies on the synthesis of SBA-15 using different surfactants, silica sources and reaction conditions (temperature, time, pH value, etc.). They yielded SBA-15 materials with BET surface areas between 630 and 1040  $\text{m}^2/\text{g}$ , pore sizes ranging from 4.7 to 10 nm and wall thicknesses of 3.4 to 6.4 nm. They revealed that the pore size of SBA-15 and the thickness of the silica walls can be adjusted by varying the temperature (35 to 140  $^\circ\text{C}$ ) and duration (11 to 72 h) of the aging process,

### 3 Experimental

which occurs after the silica source is added to the dissolved block copolymer. Higher temperatures and longer reaction times produced larger pores and thinner silica walls. The triblock copolymers poly(ethylene oxide)-poly(propylene oxide)-poly(ethylene oxide) PEO-PPO-PEO showed good ordering properties, amphiphilic character and biodegradability, and were commercially available cheaply. Varying the EO:PO ratio affected the morphology of the obtained material [50, 51]. Lower ratios favoured the hexagonal morphology (p6mm), which was the desired structure in this thesis. The concentration of block copolymer and the pH-value during synthesis both influenced the properties of the SBA-15. Concentrations of block copolymer higher than 6 wt% produced only silica gel, whereas concentrations below 0.5 wt% yielded amorphous silica. At  $\text{pH} < 1$  hexagonal mesoporous SBA-15 was formed. At pH-values between 2 and 6, no precipitation or formation of silica gel occurred, whereas neutral pH lead only to disordered or amorphous silica.

#### 3.1.1.2 Procedure

4 g of the block copolymer surfactant  $\text{PEO}_{20}\text{PPO}_{70}\text{PEO}_{20}$  (Pluronic P123,  $M = 5880 \text{ g/mol}$ , Aldrich) was dissolved in 100 ml 2-M hydrochloric acid (HCl) and stirred at room temperature for 2 h. 11 ml tetraethylorthosilicate (TEOS, Aldrich) was then added dropwise while the solution was stirred vigorously and the mixture was then stirred at  $60 \text{ }^\circ\text{C}$  for 40 h applying an oil bath and a reflux condenser The synthesis setup is shown in Figure 3.2.

The obtained white precipitate, was then recovered by vacuum filtration, washed with DI water (800 ml) until the pH of the filtrate was neutral and dried in the fume hood overnight. Finally, the as-synthesized SBA-15 was dried in the oven at  $110 \text{ }^\circ\text{C}$  for 4 h and calcined in a kiln (AF-3, Woodrow) for 4 h at  $550 \text{ }^\circ\text{C}$  under air (heating rate =  $1 \text{ }^\circ\text{C}/\text{min}$ ) in order to remove the polymer-template.

#### 3.1.2 Synthesis of SiC

SiC was prepared via a nanocasting process using the mesoporous silica SBA-15, synthesized in Section 3.1.1 as a hard template [4, 52] polycarbomethylsilane (PCMS) as a precursor and NaOH as the etching agent [45].

##### 3.1.2.1 Method

**Nanocasting process** Nanocasting is a method of producing mesoporous materials (carbon, metals, metal oxides, etc.) by using mesoporous silicates as hard templates. Nanocasting offers incredible possibilities in preparing new mesostructures, especially

### 3 Experimental

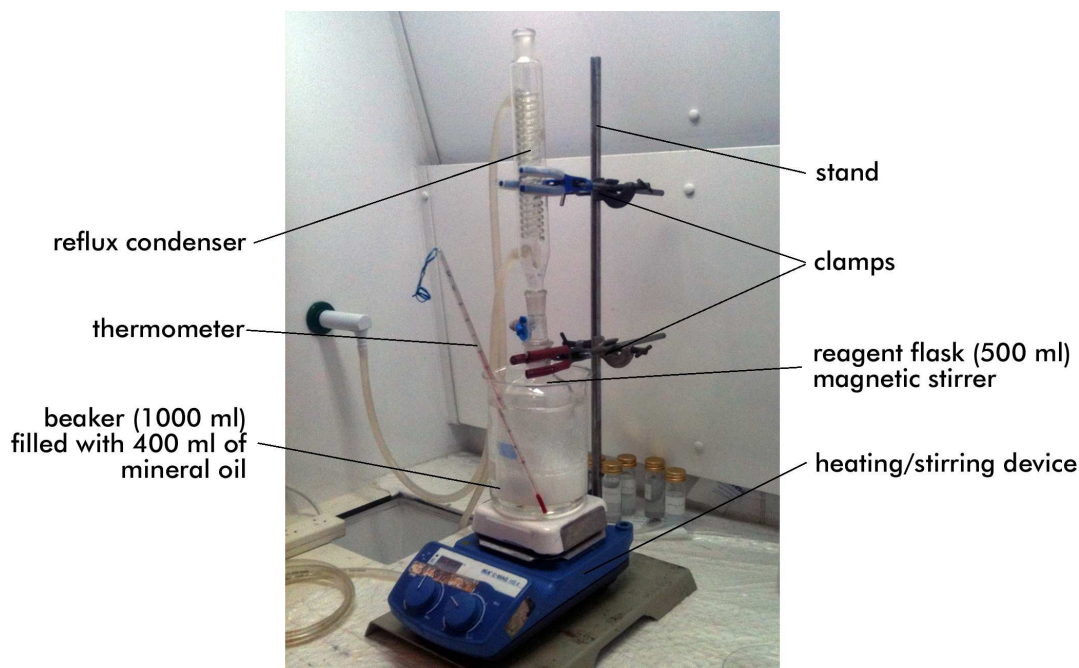
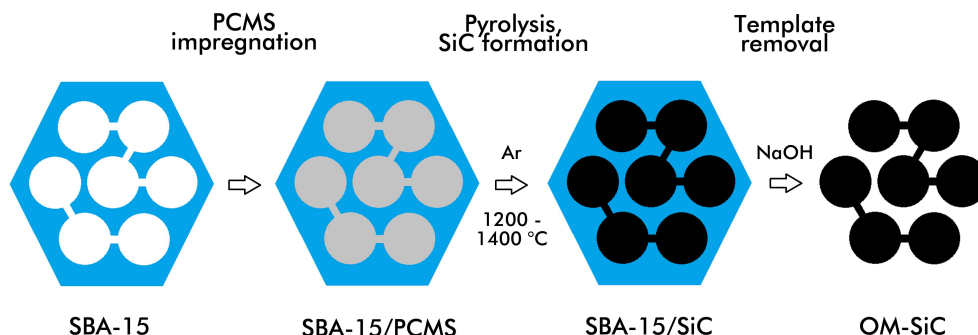


Figure 3.2 Setup of the SBA-15 synthesis.

for materials that can not be derived from sol-gel processes (Section 3.1.1). In the first step the precursor is incorporated into the channels of the mesoporous silica template; this can be achieved by different mechanisms (sorption, phase transition, ion exchange, etc.). The impregnated material is then thermally treated which causes the precursors to decompose and form nanoparticles that grow larger and larger as they connect to each other and crystallize. The process of thermal treatment is called pyrolysis, which is not to be confused with the pyrolysis process happening during the heating of, e.g. biomass, in the absence of oxygen. If the loading rate of the precursors is sufficient, the nanocrystals can interlink during the thermal treatment, and form continuous frameworks. Finally, the mesoporous silicate is removed, usually by dissolution in aqueous NaOH or HF (etching), though other process as solvent extraction or microwave digestion can be used [53]. Figure 3.3 shows the principle nanocasting procedure using the example of ordered mesoporous SiC synthesis from as SBA-15 template.

**Literature** Shi et al. [4] synthesized ordered mesoporous SiC by mixing a solution of PCMS in xylene with mesoporous silica SBA-15 or KIT-6, and using HF as the etching agent. They obtained materials with BET surface areas up to  $720 \text{ m}^2/\text{g}$ , depending on the pyrolysis temperature, the substrate and the temperature used during the aging of the silica template. The highest surface area was obtained when SBA-15, which had been hydrothermally treated at  $100 \text{ }^\circ\text{C}$ , was impregnated with PCMS and pyrolysed at  $1200 \text{ }^\circ\text{C}$ . SiC materials that were produced from templates synthesized at higher aging tem-

### 3 Experimental



**Figure 3.3** Synthesis of ordered mesoporous (OM) SiC using the nanocasting process. Re-drawn from reference [53].

peratures had smaller surface areas, bigger pore sizes (3.6 nm rather than 2.0 nm) and more highly ordered mesostructures due to the formation of microtunnels in the silica walls. An increase of the pyrolysis temperature to 1400 °C caused a slight decrease of the surface area and a distinct improvement in the crystallinity. Furthermore, a minimum pyrolysis temperature of 1200 °C was required to form SiC, below that no XRD peaks were detected. The pyrolysis procedure (heating rate, holding time and temperatures) was essential to the ceramic yield and hence for the formation of mesoporous SiC.

Krawiec et al. [52] achieved SiC with BET surface areas up to 800 m<sup>2</sup>/g using SBA-15 as a template, direct infiltration of liquid, low-molecular-weight precursors and HF as the etching agent. They also investigated a melt impregnation method and a solvent-free method in order to incorporate PCMS into the SBA-15 template.

Based on the work of Shi et al. [4] and Krawiec et al. [52], Widyawati et al.[45] synthesized mesoporous SiC as a CaO-support material for carbon capture purposes using incipient wetness impregnation (see Section 3.1.3.1) of polycarbomethylsilane (PCMS). Due to safety issues, NaOH was used instead of HF, to remove the silicate template, which led to SiC that lacked the highly ordered structure of SBA-15 and had lower surface area (470 m<sup>2</sup>/g). Nevertheless, this SiC was mesoporous, based on the shape of its N<sub>2</sub> adsorption-desorption-isotherms.

#### 3.1.2.2 Procedure

The synthesis of SiC was accomplished using the initially synthesized SBA-15 as the template, according to a literature procedure [45]. 0.727 g polycarbomethylsilane (PCMS, Aldrich) was dissolved in a mixture of 17.989 ml heptane and 0.1086 ml 1-butanol. The molarity of PCMS in the solution was 0.05 M. The amount of PCMS to be used was ca-

### 3 Experimental

culated based on the total pore volume of the silica, assuming that all of the volume was to be filled with PCMS. The ratio of heptane and 1-butanol (v/v) was 0.994 to 0.006.

The solution was added to SBA-15 which had been dried in a vacuum oven at 130 °C overnight. The resulting suspension was then stirred in a 100-ml beaker in the fume hood to vaporize the solvent, then dried in an oven at 100 °C for at least 48 h. The as-synthesized material was pyrolyzed under argon (263 ml/min) in a tube furnace (GSL 1600 - 60X, *MTI Corporation*) using a heating programme (Figure 3.4) that was based on the investigations of Shi et al. [4], who investigated the impact of the pyrolysis procedure on the ceramic yield. In order to remove the silica-temple, the obtained black-coloured sample was etched five times in respectively 100 ml of 2-M sodium hydroxide (NaOH) at 80 °C, applying an oil bath and a reflux condenser as shown in Figure 3.5. Fresh NaOH solution was used for each etching step. To recover the sample between etching steps, vacuum filtration using a membrane filter (0.45 µm FH, *Millipore*) was applied. The obtained SiC was neutralized by washing it with DI Water (600 ml) several times under vacuum filtration and then dried in a fume hood overnight and in a vacuum oven at 110 °C for 24 h.

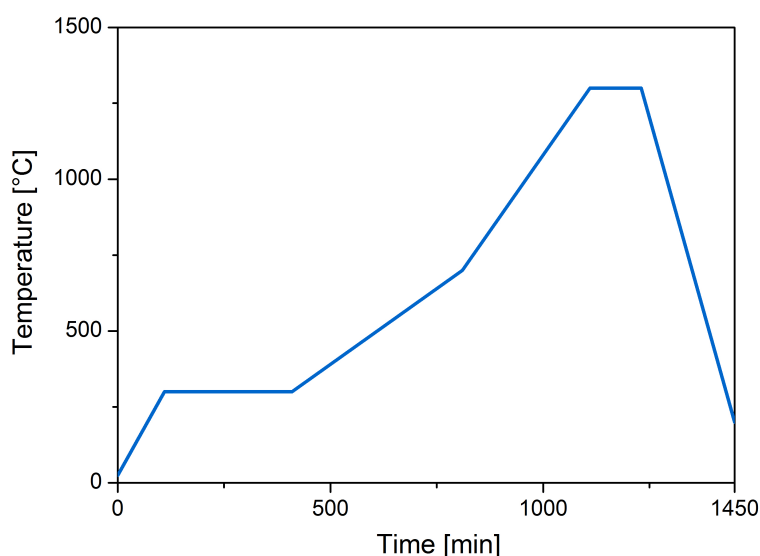


Figure 3.4 Heating programme of SBA-15/PCMS pyrolysis.

#### 3.1.3 Incorporation of metals into substrates

A modified incipient wetness impregnation technique [7] was used to incorporate nickel nitrate,  $\text{Ni}(\text{NO}_3)_2 \cdot 6\text{H}_2\text{O}$  and cobalt nitrate  $\text{Co}(\text{NO}_3)_2 \cdot 6\text{H}_2\text{O}$ , into the support materials. A total metal loading of 10 wt% and a Ni/Co ratio of 1:2 were used. This was in accordance

### 3 Experimental

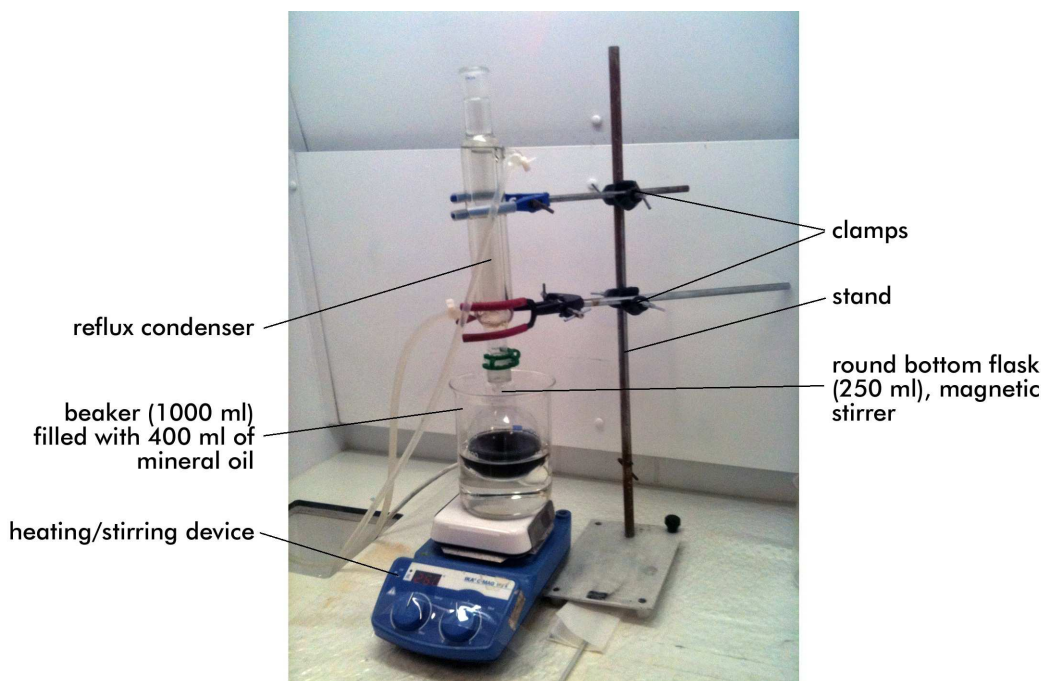


Figure 3.5 Setup of SBA-15/SiC etching.

with results of Zhao et al. [5], who investigated the hydrogen production during cellulose decomposition in the presence of SBA-15-supported Ni, Co and Ni-Co catalysts with various metal loadings. The metal salts were then degraded to their oxide forms and subsequently reduced under  $H_2$  to obtain bimetallic catalysts.

#### 3.1.3.1 Incipient wetness impregnation

The incipient wetness impregnation, also known as capillary impregnation or dry impregnation, is a common method of synthesizing solid catalysts. An active metal is dissolved in water or an organic solvent and then added to the solid catalyst support. The amount of solution is equal to the pore volume of the catalyst support. Capillary forces pull the solution into the pores if the volume of the solution does not exceed the pore volume of the used support. Excess solution causes a change in the transport mechanism to a diffusion process, which is slower than the capillary process. Following filtration, the catalyst is dried in order to evaporate the volatile components within the solution, and calcined to achieve further conversion of the impregnated species. The maximum metal loading depends on the solubility of the metal in the solution [54].

#### 3.1.3.2 Procedure

300 mg each of SBA-15 and SiC, respectively, were dried for 4 h at 150 °C in a vacuum oven in order to produce clean inner surfaces on the substrate. 54.3 mg  $Ni(NO_3)_2 \cdot 6H_2O$

### 3 Experimental

(Aldrich) and 110.0 mg  $\text{Co}(\text{NO}_3)_2 \cdot 6\text{H}_2\text{O}$  (Aldrich) were then dissolved in 3 ml of EtOH. The solution was poured over the support material, which sat in a small ceramic bowl, and the bowl was shaken using a mechanical shaker working at 20 Hz at room temperature for a couple of hours until only a dry powder remained. The ceramic bowl was attached to the shaker using scotch tape. The metal salts that had been incorporated into the support material were then transformed into their oxide forms by calcination (Kiln AF-3, Woodrow) at 600 °C for 4 h at a heating rate of 1 °C/min. The calcined catalyst was reduced in a thermogravimetric analyzer (SDT Q600, TA Instruments) under 25 vol.%  $\text{H}_2$  added to 300 ml/min Argon by heating at 10 °C/min to 800 °C and holding for 1 h. After reducing, the catalysts The finished catalysts were labelled 10wt.%NiCo<sub>2</sub>/SBA-15 and 10wt.%NiCo<sub>2</sub>/SiC.

## 3.2 Characterization of catalysts

### 3.2.1 Surface area, pore volume and pore size distribution

In order to determine the surface area, the pore volume and the pore size distribution of the blank support materials and impregnated catalysts their  $\text{N}_2$  adsorption-desorption isotherms (relation between the amount of nitrogen adsorbed at 77 K, the temperature of liquid nitrogen, and the equilibrium pressure) were determined. The surface area was calculated, using the Brunauer-Emmett-Teller (BET) method [55] and the pore size distribution was derived based on the Barrett-Joyner-Halena (BJH) model [56].

#### Procedure

The samples were tested in a *Quantachrome Autosorb iQ*. Two-thirds of the designated section of the measurement cell, which had been dried in the oven overnight, was filled with sample. To prevent inaccurate results, the residual particles of sample were cleaned from the inner tube surface. Before running the actual analysis, the sample was degassed for 150 min at 180 °C (heating rate = 20 °C/min). After this period the outgassing progress was checked by the instrument at 30-min intervals. For each test valves of the degas station were closed for 1 min, and the pressure before and after this period were compared. An increase in pressure implied that the sample continued to release gases, whereas a consistent pressure indicated that the degassing was complete. A critical pressure rise of 25 mTorr was set.

After passing the test, the tube was refilled with  $\text{N}_2$  and transferred to the analysis port where the adsorption-desorption isotherms at the temperature were measured (20 point

### 3 Experimental

were measured for each). From the isotherms the BET surface area, as well as the total pore volume and the BJH pore size distribution were derived. The surface area was derived from the first five points of the adsorption curve [55] ( $P/P_0=0.05-0.25$ ), the pore size distribution was calculated from the desorption curve [57]. The total pore volume was derived from the amount of vapour adsorbed at the point determined at the highest relative pressure [57].

#### 3.2.2 Crystalline structure and chemical compound

To investigate the crystalline structure, wall thickness and the chemical composition of the catalysts and the supporting materials, X-ray diffraction techniques were used. These X-Ray diffraction techniques, also known as X-ray scattering techniques, take advantage of the physical phenomenon of *Bragg diffraction* [58]. When electromagnetic waves hit a crystal lattice whose spacing matches the wavelength of the incident beam, diffraction occurs. The incident beam encourages the atoms to radiate electromagnetic waves of the same frequency itself (*elastic scattering* or *Rayleigh scattering*). Relative to the angle (*Bragg angle*) of the incident beam, which is increase stepwise over the course of the measurement, the scattered waves undergo destructive or constructive interference, which lead to extinction and amplification of the waves, respectively. The amplified waves, collected by a detector, yield a diffraction pattern characteristic of the analyzed sample [59].

#### Procedure

The XRD patterns were determined on a *Siemens* D5000 powder diffractometer using Cu  $K\alpha$  radiation with a wavelength of  $\lambda=0.1542$  nm. Wide angle X-ray scattering (WAXS) patterns of the catalysts (in oxidized and reduced form) were measured over  $2\theta=10-75^\circ$  with an interval size of  $0.02^\circ$ . Small angle X-ray patterns (SAXS) of the SiC support, over  $2\theta=2-10^\circ$  with a step interval of  $0.005^\circ$ , were determined using the same facility. The specimens were prepared by grinding, with a clean mortar and pestle to reduce the particle size in order to achieve accurate measuring. The powder was then placed in a sample holder and spread flat using a razor blade.

The average wall thickness of the support material was calculated by subtracting the most common pore size, calculated using the BJH method (see Section 3.2.1), from the *d-spacing* calculated via the Bragg equation (Equation 3.2) [58].

$$n\lambda = 2d\sin\theta \quad (3.2)$$

Herein  $n$  is an integer,  $\lambda$  the wavelength of the incident radiation,  $d$  the distance between similar crystal planes (W. L. Bragg modelled the crystal as a set of parallel planes sepa-

### 3 Experimental

rated by a constant parameter  $d$ , off which the incoming waves were reflected [58].) and  $\theta$  the Bragg angle, i.e. the angle between the incident wave and the scattering plane.

A SAXS instrument (SAXSess, Anton Paar) was used to examine the ordered pore structure of the blank SBA-15 using Cu  $K\alpha$  radiation ( $\lambda=0.1542$  nm). The SAXS instrument was used because the structure of SBA-15 has inhomogeneities about 5 nm apart, which gives a Bragg angles of about  $0.5^\circ$ . The Siemens D5000 instrument is not capable of working at such small angles. As with XRD samples, the samples used for SAXS analysis were ground using a mortar and pestle. Subsequently the powder was placed between two strips of scotch tape, which were then cut to fit the dedicated sample holder. The SAXS patterns were examined over  $2\theta=0.5-5^\circ$ .

As there are no moving parts in the SAXS instrument, and the Bragg angle therefore can not be derived from the position of a goniometer, the SAXS instrument measures the intensity as a function of the scattering vector

$$q = \frac{4\pi\sin(\theta)}{\lambda} \quad (3.3)$$

where  $\theta$  is the Bragg angle and  $\lambda$  is the wavelength of the the X-rays.  $\theta$  can be calculated from this equation and integrated into Bragg's Law (Equation 3.2), which then can be solved to determine the desired  $d$  spacing. [60]

### 3.2.3 Surface morphology and pore structure

#### 3.2.3.1 Scanning electron microscopy SEM

The surface morphologies of the catalysts and support materials were examined using scanning electron microscopy (Zeiss Ultra+ FESEM), scanning a sample with a beam of electrons in a raster scan pattern. The energy exchange between the electron beam and the atoms at or near the surface of the specimen causes (i) the emission of secondary electrons by inelastic scattering, (ii) the emission of electromagnetic radiation (e.g. X-rays) and (iii) the reflection of high-energy electrons by elastic scattering (producing back-scattered electrons, BSE). Each of these can be detected by specialized detectors, and various properties, like surface topography, composition and electrical conductivity, can be explored [61].

In order to prepare the sample for SEM analysis, it was ground using mortar and pestle and subsequently placed on a piece of carbon tape that was stuck to the sample holder. To obtain accurate results, the sample holder was not to be touched by hand, but rather with pincers.

### 3 Experimental

#### 3.2.3.2 Transmission electron microscopy TEM

To assess the inner pore structure of the support materials and as the distribution of the metal sites on them, transmission electron microscopy (CM120 BioFilter, *Philips*) was employed. The scattering of an electron beam upon passing through a specimen, depends on the ordinal number of the atom and the thickness of the radiated area. The scattered electrons are detected, yielding an image that is then magnified and focused onto an imaging device [61].

A few milligrams of sample were finely dispersed in ethanol in a 20-ml glass beaker by sonicating for about one minute. The dispersion was then dripped onto a copper grid (strong carbon film, 200 mesh, *ProSciTech*) which was placed on filter paper using a glass pipette.

#### 3.2.4 Active surface area

To analyse the active surface area of the reduced metal catalysts, as well as the dispersion and average crystallite size of the metal sites of the catalysts, H<sub>2</sub> chemisorption was used. These experiments were conducted using the same instrument that was used for the physisorption experiments (see Section 3.2.1). Chemisorption is basically the adsorption of gas molecules on the surface area of a solid, whereby the connection of the surface area and the molecules is achieved by chemical bonds, rather than by van der Waals forces (as it is the case in physisorption). During a chemisorption experiment, three curves, the combined (chemisorption & physisorption), strong (chemisorption) and weak (physisorption) curves are measured, by recording the adsorbed volume of a reactive gas vs. its partial pressure (which was increased stepwise from 40 to 760 mmHg). From the chemisorption isotherm the monolayer chemisorbed volume can be derived by extrapolation to P=0 [62]. From this value, the active surface area and the average crystal size of the metal sites can further be calculated [6].

##### 3.2.4.1 Procedure

100 mg of catalysts was loaded into the measurement cell between two layers of cotton wool. Before running the actual experiment, the sample was degassed by heating it to 180 °C and maintaining the temperature for 150 min using an electrical heating device. The degassed sample was then evacuated for 30 min and subsequently heated up at 50 °C/min to 800 °C under 100 ml/min hydrogen. The hydrogen flow was maintained for 60 min in order to remove all species chemisorbed on the sample surface. The sample was then cooled down to 50 °C and the electrical heating device was replaced with a water bath. The H<sub>2</sub> chemisorption isotherm was determined at 30 °C (water bath) a pressure

### 3 Experimental

range of 0 to 760 mmHg after an equilibration time of 30 min.

#### 3.2.4.2 Evaluation

The parameters calculated from the chemisorption experiments were obtained using the extrapolation method on the combined adsorption branch over 0-480 mmHg. To facilitate the calculations only the structural parameters for Ni were used, thus it was assumed that all metal atoms were the size and shape of Ni atoms. The presence of two different metals was not taken into account. It was furthermore assumed, that the reaction stoichiometry was  $2\text{Ni} + \text{H}_2 \rightarrow 2\text{NiH}$  and that the metal loading was exactly 10 wt%.

### 3.3 Testing of Catalysts

The performance of the catalysts was tested by decomposing cellulose in their presence, in a modified thermogravimetric analyzer (TGA) coupled with a mass spectrometer (MS). The apparatus has been described by Florin and Harris [63, 64], who studied the influence of different process parameters (heating rate, loading, residence time, reaction atmosphere) on the hydrogen yield in biomass gasification with in situ  $\text{CO}_2$  capture using CaO. Cellulose (methyl cellulose, *Aldrich*) was used as the biomass substitute, as it is the main component in biogenic solid fuels (up to 50 wt.%), which also contains hemicellulose, lignin, resins/fats and ash [22], and the main gasification products can be correlated to the cellulose content [64].

#### 3.3.1 Apparatus

The experiments were carried out using a SDT Q600 thermogravimetric analyzer (*TA Instruments*) coupled with a ThermoStar GSD301 mass spectrometer (*Pfeifer Vacuum*), which is shown in Figure 3.6. The TGA measured the weight loss of the analyzed sample during pyrolysis and gasification using a thermobalance sensitive to 0.01 mg. The gas species generated during decomposition were purged away from the reaction zone by an argon stream (500 ml/min) and lead to the mass spectrometer through a heated capillary (200 °C). The MS measured the mass spectrum for the evolved gases repeatedly so that it could be considered as a function of the temperature of decomposition.

In a mass spectrometry analysis, the gas molecules are bombarded with an electron beam, which produces positively charged molecular ions. These ions are then accelerated through an electronic field and sorted, depending on their mass-to-charge ratio  $m/z$ . As the electron beam energy is usually greater than the energy needed to achieve ionization, fragmentation of the primary molecular ions can occur [65].

### 3 Experimental

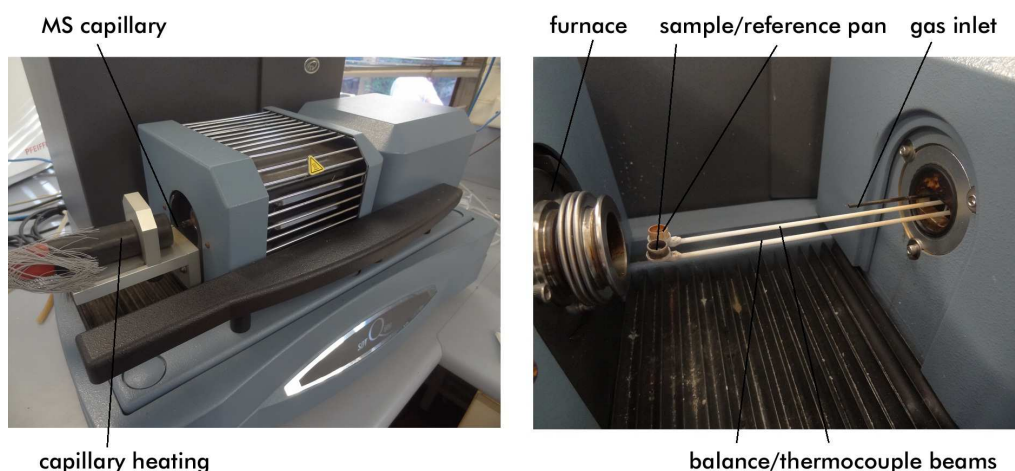


**Figure 3.6** TGMS used for the testing of the catalysts. Right: TGA in closed position with connected MS; Left: opened TGA.

#### 3.3.2 Experiment

5 mg of well-mixed cellulose-catalyst samples (mass ratio 1:1), prepared immediately after catalyst reduction, were loaded into the tared alumina pan inside the TGA. A small amount of sample was used to achieve reproducible kinetic data [64], limit heat- and mass-transfer effects and minimize the risk of blocking the capillary with condensed tars [7]. In order to remove air and any other potential contaminants from the reaction zone, stabilize the balance and achieve a steady MS-signal the TGA was purged with argon for one hour prior to the start of the actual experiment. Subsequently the sample was heated at 40 °C/min to 800 °C. During this step, the sample decomposed and the evolved gases were lead to the MS, which recorded the  $m/z$  values<sup>2</sup> of the various species/fragments (Table 3.1). In the last step, the residues located on the TG pan was burned in air by heating up the furnace from 800 to 950 °C at 20 °C/min, then maintaining that temperature for 6 h in order to remove all combustible components.

For molecular ions/ion fragments with  $m/z > 55$  only small signals with intense background noise were found, which indicates that heavier fragments like tars were evolved only in very small amounts, or not transported to the MS [7]. Ions/ion fragments with  $m/z > 100$  were not recorded.

<sup>2</sup>The  $m/z$  number is the mass-to-charge ratio recorded by a mass spectrometry, where  $m$  stands for the mass of an ion and  $z$  for the number of elementary charges carried by this ion

### 3 Experimental

m/z	Key ions/ion fragments	Representative species
2	H <sub>2</sub> <sup>+</sup>	Hydrogen
15	CH <sub>3</sub> <sup>+</sup>	Methane
18	H <sub>2</sub> O <sup>+</sup>	Water
26,27,41,42,43,55	C <sub>2</sub> H <sub>2</sub> <sup>+</sup> , C <sub>2</sub> H <sub>3</sub> <sup>+</sup> , C <sub>3</sub> H <sub>5</sub> <sup>+</sup> , C <sub>3</sub> H <sub>6</sub> <sup>+</sup> , C <sub>3</sub> H <sub>7</sub> <sup>+</sup> , C <sub>4</sub> H <sub>7</sub> <sup>+</sup>	Hydrocarbons
28	CO <sup>+</sup>	Carbon monoxide
29	CHO <sup>+</sup>	Aldehydes
30	CH <sub>2</sub> O <sup>+</sup>	Formaldehyde
31,45,46	CH <sub>2</sub> OH <sup>+</sup> , C <sub>2</sub> H <sub>5</sub> O <sup>+</sup> , C <sub>2</sub> H <sub>5</sub> OH <sup>+</sup>	Alcohols
44	CO <sub>2</sub> O <sup>+</sup>	Carbon dioxide

**Table 3.1** Key molecular ions/ion fragments and probable representative molecules [7].

#### 3.3.3 Evaluation

The experiments were evaluated using a semi-quantitative analysis method published by Zhao et al. [7] and thus does not give absolute, quantitative yields. The method facilitates the comparison of similar experiments, as conducted in this work.

Due to fluctuations of the MS signal throughout the different experiments, the raw MS data was normalized relative to the stable m/z signals of Argon (IC<sub>20</sub> and IC<sub>40</sub>), the constant flow rate of Argon and the weight of cellulose; the mean value of the cellulose weight recorded by the TGA during the last 10 minutes before the start of the actual experiment was used. The formation rate of species *i*, stated as *f<sub>i</sub>*, in (ml/g cellulose) was calculated according to Equation 3.4.

$$f_i = \frac{IC_i}{IC_{20} + IC_{40}} \times \frac{\dot{v}_{Ar}}{m_C} \quad (3.4)$$

where IC<sub>*i*</sub> stands for the ion-current signal of species *i* (arbitrary unit) and IC<sub>20</sub> and IC<sub>40</sub> for the m/z signals of argon,  $\dot{v}_{Ar}$  the flow rate of Ar in ml/min and *m<sub>C</sub>* the mass of cellulose in g. The obtained generation rate was subsequently plotted as a function of reaction temperature and then integrated between 200 and 600 °C (period in which of degeneration in almost all of the gas yield occurred, see Figure 4.10) in order to obtain the cumulative gas yields.

## 4 Results and discussion

### 4.1 Characterization of support materials and catalysts

Figures 4.1 and 4.2 show the adsorption-desorption isotherms of the supports, SBA-15 and SiC, as well as the bimetallic catalysts NiCo<sub>2</sub>/SBA-15 and NiCo<sub>2</sub>/SiC. All isotherms reveal hysteresis loops that were associated with the Type IV isotherm, according to the classification of the International Union of Pure and Applied Chemistry, IUPAC (Figure 4.3)<sup>1</sup>. This type of isotherm, indicates the presence of mesopores, which were desired in order to facilitate the uptake of larger molecules evolving during the gasification process [57]. The different shapes of hysteresis loops revealed by the various isotherms are indicative of the diverse inner structures of the investigated support materials and catalysts.

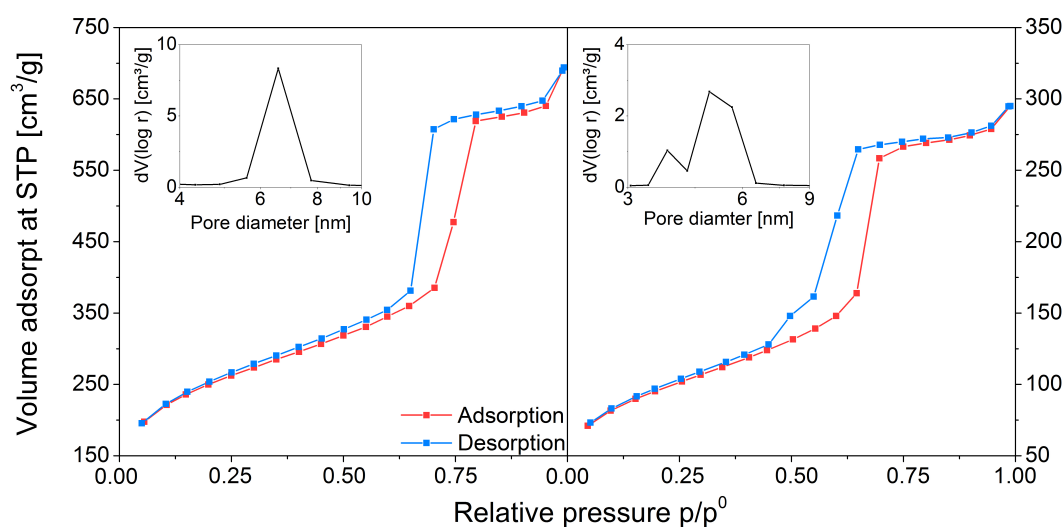


**Figure 4.1** Adsorption-desorption isotherms of the SBA-15 substrate (left), and the bimetallic NiCo<sub>2</sub>/SBA15 catalyst (right).

SBA-15 yielded a hysteresis with almost vertical and nearly parallel branches over a small range of high relative pressures (Figure 4.1, left). This is defined as a Type H1 hysteresis, according to the classification of the IUPAC (Figure 4.3), evincin the highly ordered

<sup>1</sup>The IUPAC is the leading institution upon the introduction of standards, normalised terminioliges or measurements, etc. and was found to facilitate the communication between chemists all over the world.

#### 4 Results and discussion

structure of the silica and a narrow pore size distribution, which is further confirmed by the distinct peak in the BJH pore size distribution that is shown in the small diagram incorporated in Figure 4.1. The well-defined order of the SBA-15 together with the narrow pore size distribution resulted in a very high surface area of 887.4 m<sup>2</sup>/g, a total pore volume of 1.07 cm<sup>3</sup>/g and an average pore diameter of about 6.5 nm (Table 4.1).

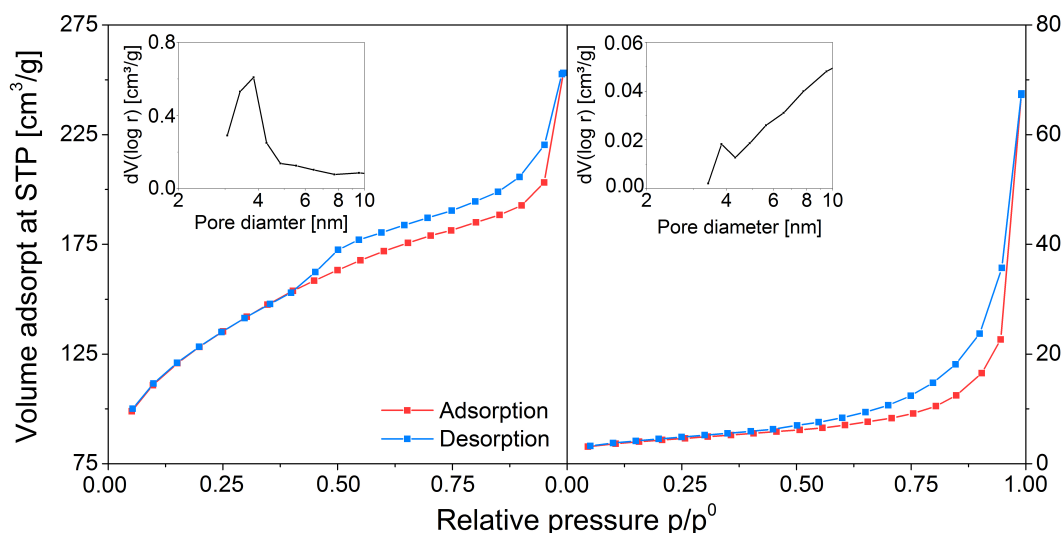


**Figure 4.2** Adsorption-desorption isotherms of the SiC substrate (left) and the bimetallic NiCo<sub>2</sub>/SiC catalyst (right).

After Ni and Co were impregnated into SBA-15, the surface area and the total pore volume decreased by more than 50% to 333.4 m<sup>2</sup>/g and 0.46 cm<sup>3</sup>/g, respectively, which was most likely due to the partial blockage of pores by metal particles. The hysteresis loop had a slightly different shape compared to the one measured for SBA-15, but was still a Type H1 hysteresis, and thus associated with a well-ordered structure. The shape suggests a disrupted pore size distribution, which is confirmed by the BJH pore size distribution, which contained a main peak at about 5.2 nm and a secondary peak at 3.8 nm.

Sample	SA [m <sup>2</sup> /g]	PV [cm <sup>3</sup> /g]	APD [nm]
SBA-15	887.4	1.07	6.5
NiCo <sub>2</sub> /SBA-15	333.4	0.46	5.2*, 3.8**
SiC	450.9	0.39	3.9
NiCo <sub>2</sub> /SiC	15.4	0.10	3.9***

**Table 4.1** Physisorption results of blank support materials and catalysts. (SA) BET Surface Area, (PV) Pore Volume, (APD) Average Pore Diameter. \* main peak, \*\* secondary peak, \*\*\* small, indistinct peak, no dominant pore size.

The hysteresis loop obtained from the SiC substrate (Figure 4.2) showed a Type H4 char-

#### 4 Results and discussion

acter, revealing almost horizontal branches over a large range of relative pressures. In contrast to the Type H1 hysteresis shown by the SBA-15 substrate, this indicates that the SiC had a less-ordered structure, a broader pore size distribution and the narrow-slit-like pores [57]. The narrow hysteresis loop further indicates smaller pores than those present in the SBA-15. Both the narrow pore size distribution and the smaller pore size, compared to the SBA-15 substrate, were confirmed by the BJH pore size distribution (Figure 4.2, inset), which showed a peak at about 3.9 nm. The lack of order lead to a smaller surface area ( $450.9 \text{ m}^2/\text{g}$ ) and pore volume ( $0.39 \text{ cm}^3/\text{g}$ ) for the SiC than for the silica.

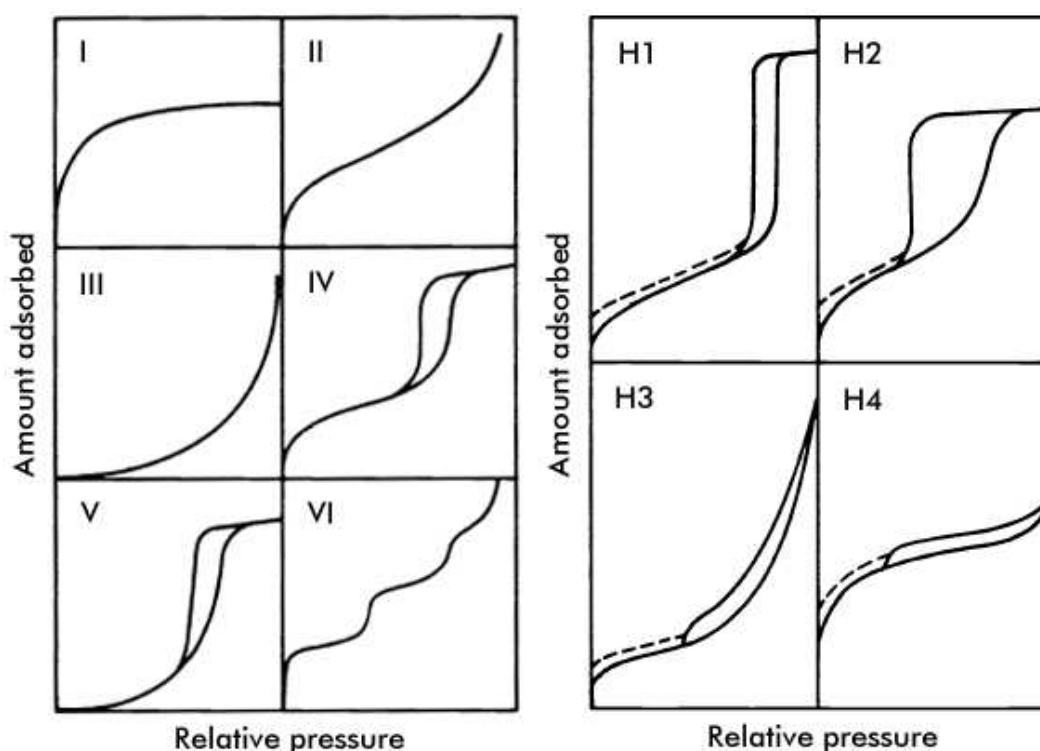


**Figure 4.3** Classification of adsorption-desorption isotherms (left) and hysteresis loops (right) according to the IUPAC. Reproduced from reference [57].

Incorporating the metals into SiC caused a tremendous drop of the surface area, to  $15.4 \text{ m}^2/\text{g}$ , which was most likely due to the blockage of many pores by metal sites; this would have been facilitated by the smaller pore size of SiC. Despite small surface area, the isotherm of this material contained a hysteresis loop that indicated some mesopores were present. The hysteresis (Figure 4.2, left) was Typ H3 which indicates, that aggregates of plate-like particles gave rise to slit-shaped pores [57]. The BJH pore size distribution of the  $\text{NiCo}_2/\text{SiC}$  rises continuously, with only a tiny peak at 3.9 (at the same position as shown in the BJH pore size distribution of the SiC substrate). This lack of a dominant pore size, further supports the assumption that a big fraction of the pores was blocked

## 4 Results and discussion

by metal particles.

The conclusions drawn from the adsorption-desorption isotherms regarding the internal structure of the supports, SBA-15 and SiC, were confirmed by the small-angle XRD patterns, displayed in Figure 4.4, as well as by the results of TEM and SEM analyses (Figures 4.5, 4.6 and 4.8). The XRD pattern of SBA-15 (Figure 4.4, left), displayed the reported peaks for the crystal planes (see Section 3.2.2) of SiO<sub>2</sub> with the *Miller-Indices* (100), (110) and (200), indicating a highly-ordered hexagonal structure of silica [50]. The pattern of SiC (Figure 4.4, right) lacked such peaks and hence low range order. This indicates that the well-defined structure of the silica template used to synthesize the mesoporous SiC, was not preserved during the synthesis. This was most likely due to use of NaOH as the etching agent [45], as other groups have achieved the synthesis of well-ordered mesoporous SiC using the same synthesis, but with HF instead of NaOH as the etching agent [4, 52].

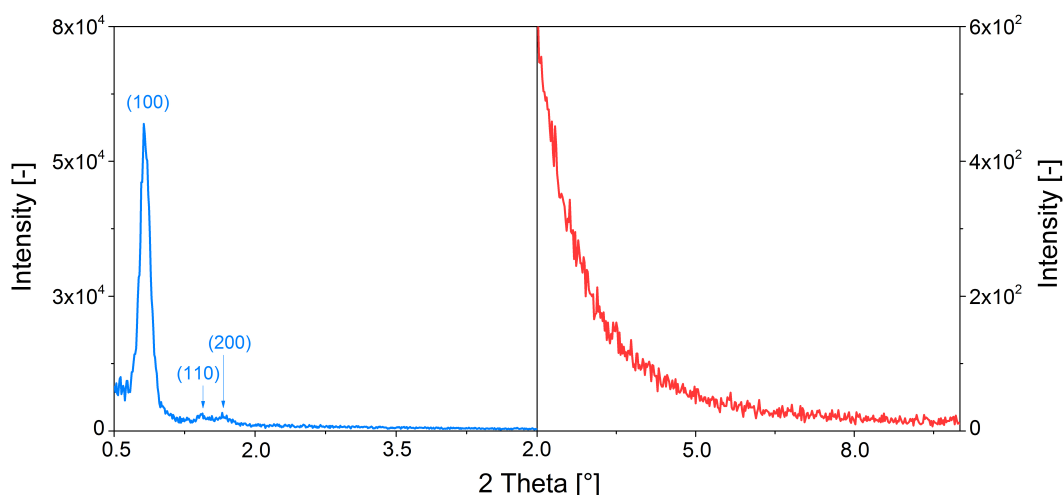


**Figure 4.4** Small-angle X-ray diffraction patterns of the blank supports, SBA-15 (left) and SiC (right).

Figure 4.5 shows the transmission electron microscopy images of the substrates and catalysts. The blank SBA-15, as shown in images (i) and (ii), as well as the catalyst NiCo<sub>2</sub>/SBA-15 (iii) revealed highly ordered, two-dimensional hexagonal structures with mesopores of about 6 nm, consistent with the pore size derived from the BJH pore size distribution (Table 4.1). This ordered structure was obviously destroyed during the synthesis of SiC, as neither the SiC support nor the NiCo<sub>2</sub>/SiC showed any kind of order at all. Images (iii) and (vi) show the even distribution of metal sites (shown as black dots) on both substrates. The Ni-Co particles on NiCo<sub>2</sub>/SBA-15 (iii) varied strongly in terms of size. The bigger particles were most likely located on the outer surface of NiCo<sub>2</sub>/SBA-15,

#### 4 Results and discussion

whereas the smaller particles were most likely spread over the inner surface (pores) of the support material, where their growth would have been limited by the narrow pores. NiCo<sub>2</sub>/SiC (vi) showed little distinct variations in terms of particle size. Nevertheless the TEM image itself, cannot show whether the particles were located on the outer or inner surface of the catalyst, as the domains assessed in the micrographs may be an overlap of several atomic layers. To assess the distribution of the metal particles on and inside the catalysts, chemisorption experiments were conducted. The results can be found at the end of this section.

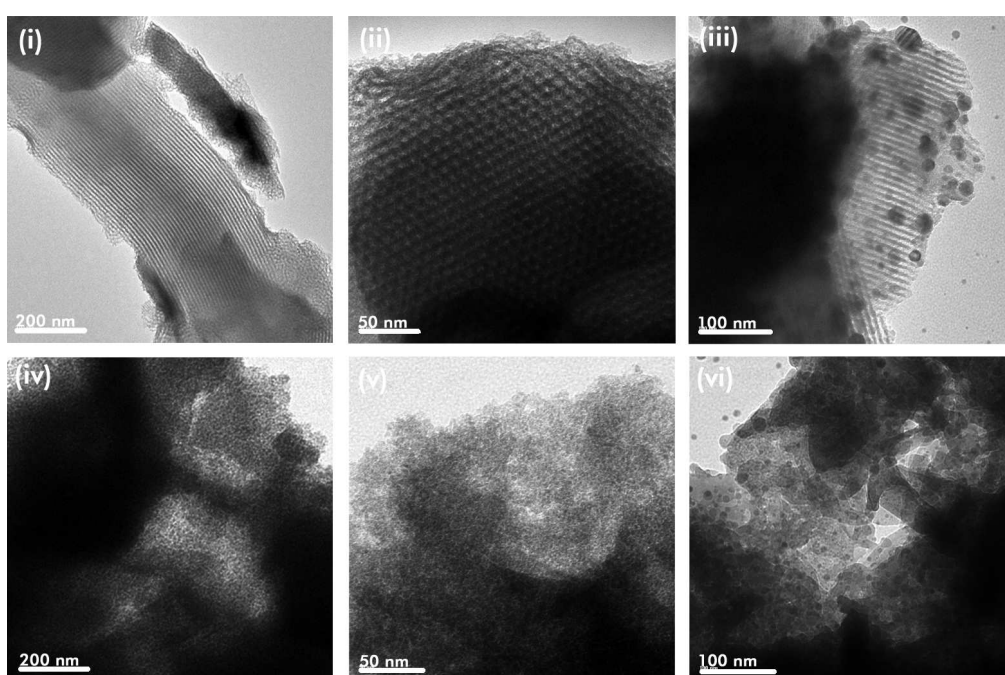


**Figure 4.5** Transmission electron microscopy images of the blank supports and the reduced catalysts: (i) and (ii) SBA-15, (iii) NiCo<sub>2</sub>/SBA-15, (iv) and (v) SiC, (vi) NiCo<sub>2</sub>/SiC.

Scanning electron micrographs of SBA-15 (i) and NiCo<sub>2</sub>/SBA-15 (ii) are shown in Figure 4.6, and reveal the bundled, rope like structure of the samples. The macroscopic structure was retained after impregnation with Ni and Co and calcination at 600 °C for 4 h, indicating the high thermal stability of the SBA-15 with and without metal loading. The texture of the SBA-15 template was partially conserved in SiC (iii) and NiCo<sub>2</sub>/SiC (iv), although it was destroyed in very large regions of the sample, as displayed in Figure 4.7. This figure compares the texture of as-synthesized SiC before (i) and after (ii) the removal of the silica template by etching in NaOH. The morphology before etching was almost identical to that of SBA-15 (Figure 4.6, i). After etching the structure no longer matched that of silica, supporting the hypothesis made, based on the XRD patterns, that the loss of order occurred during the etching process.

#### 4 Results and discussion

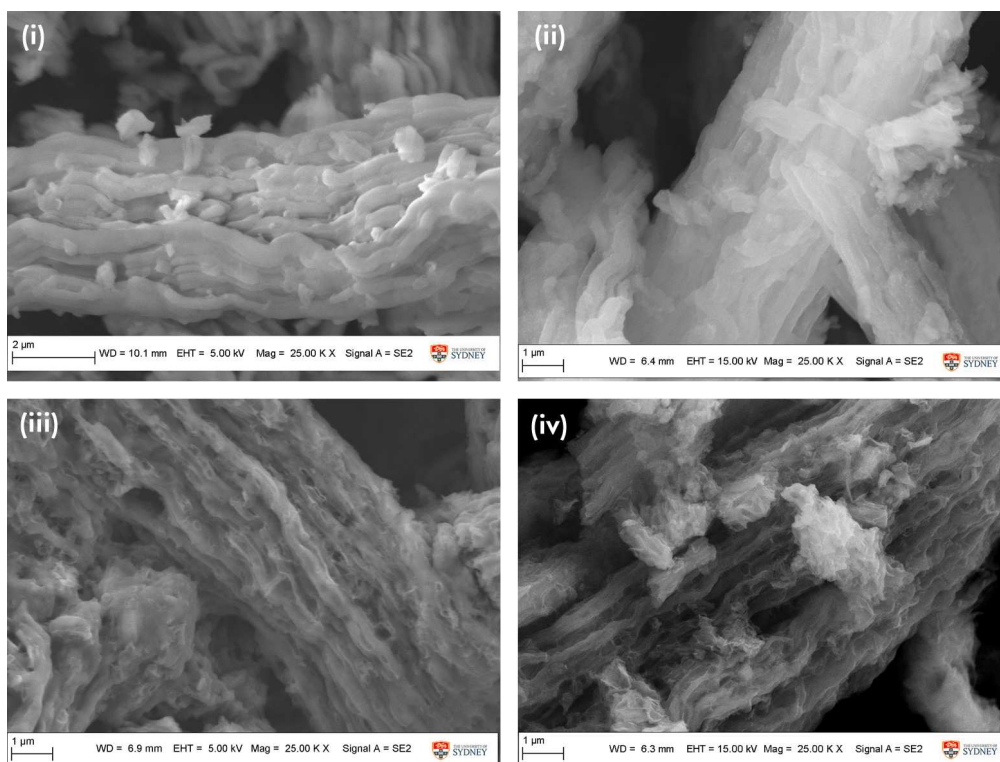


**Figure 4.6** Scanning electron microscopy images of the blank supports and the reduced catalysts: (i) SBA-15, (ii) NiCo<sub>2</sub>/SBA-15, (iii) SiC, (iv) NiCo<sub>2</sub>/SiC.

SEM images at higher magnification, shown in Figure 4.8, reveal evenly distributed metal sites on the outer surfaces of both, NiCo<sub>2</sub>/SBA-15 (i) and NiCo<sub>2</sub>/SBA-15 (ii). The SBA-15-supported catalyst exhibits bigger Ni-Co crystallites than the SiC-supported one, which would suggest NiCo<sub>2</sub>/SiC had a higher surface area than NiCo<sub>2</sub>/SBA-15.

This was not consistent with the chemisorption results (Table 4.2), which were almost similar for both catalysts, and revealed big average crystallite sizes of about 70 nm and small active surface areas of less than 1 m<sup>2</sup>/g at 30 °C. As SBA-15 had much bigger BET surface area and pore size than SiC more dispersion was expected for SBA-15 supported catalyst compared to SiC supported one. This, together with the big average crystallite size for both catalysts, which is more than 10 and 20 times bigger than the average pore size of the NiCo<sub>2</sub>/SBA-15 and NiCo<sub>2</sub>/SiC catalysts, respectively, indicates that the bulk of the metal particles was spread on the outer surface of the support materials rather than on the inner surface, and thus their growth was not limited by the pores. In order to check the data obtained at 30 °C, where a saturated monolayer adsorption had perhaps been far from achieved, and thus lower surface areas and metal dispersions may have been obtained, the chemisorption experiment for the NiCo<sub>2</sub>/SBA-15 catalyst was repeated at

#### 4 Results and discussion

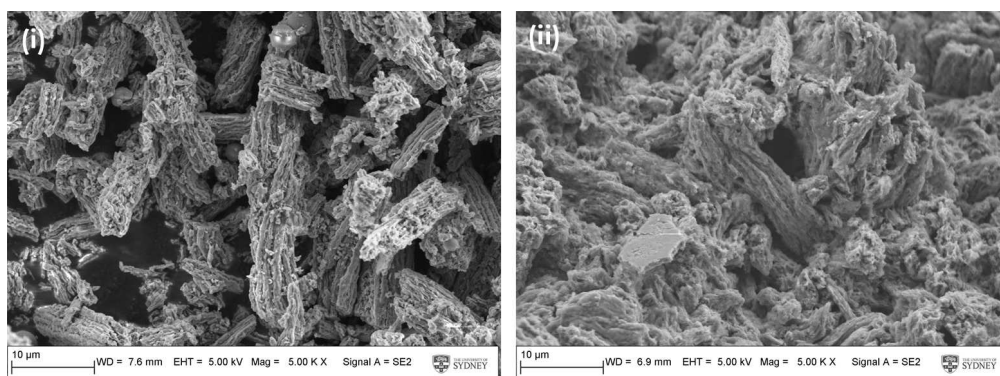


**Figure 4.7** Scanning electron microscopy images of as-synthesized  $\text{NiCo}_2/\text{SiC}$ : (i) before etching, (ii) after etching.

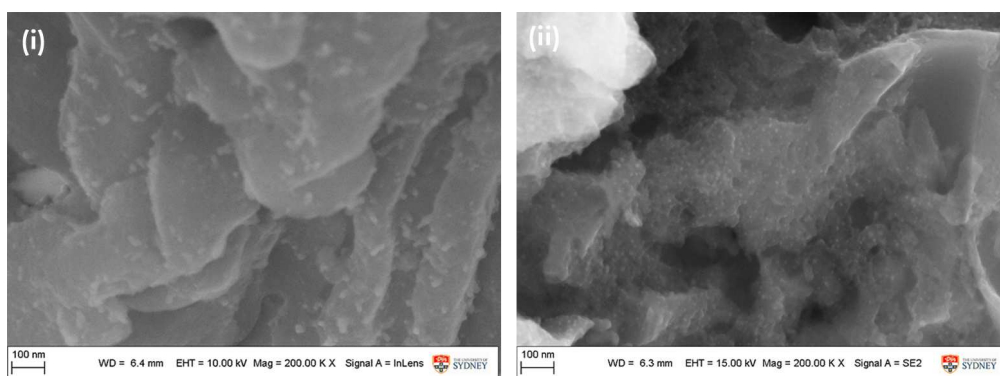


**Figure 4.8** Scanning electron microscopy images of the reduced catalysts: (i)  $\text{NiCo}_2/\text{SBA-15}$ , (ii)  $\text{NiCo}_2/\text{SiC}$ .

## 4 Results and discussion

a higher temperature of 75 °C. Slightly higher surface area, metal dispersion- and monolayer chemisorbed volume were measured, as was a reduce in crystallite size (Table 4.2), but the results still indicated, poor metal distribution on the inner surface of the catalyst. Although all of these results were based on ideal assumptions (see Section 3.2.4) and might therefore not be very close to the true values, they imply that the impregnation of the metals into the catalysts was less extensive than was intended.

Catalyst	T [°C]	ACS [nm]	MCV [μmol/g]	ASA [m <sup>2</sup> /g]	MD [%]
NiCo <sub>2</sub> /SBA-15	30	69.97	12.316	0.963	1.446
	75	56.3	15.32	1.21	1.80
NiCo <sub>2</sub> /SiC	30	75.64	11.393	0.891	1.337

**Table 4.2** Chemisorption results of the catalysts. (T) Temperature of chemisorption measurement, (ACS) Average Crystallite Size, (MCV) Monolayer Chemisorbed Volume, (ASA) Active Surface Area, (MD) Metal dispersion.

### 4.2 Catalyst testing

The decomposition of biomass in a gasification process is a complex mechanism of various chemical reactions that take place simultaneously and are massively dependent on the used operating conditions and any catalysts present. The same is true for cellulose, which was chosen as the biomass substitute in this work, because it is the major component in most of the biomass fuels used in gasification processes [22]. The depolymerization of the linear chains of (1,4)-D-glucopyranose units can follow various pathways, so an exact mechanism is hard to determine. Nevertheless, a general route of decomposition, proposed by Zhao et al. [7, 6, 5], can be written as



where DP is the degree of polymerisation of cellulose. The main reactions between the species evolved are listed in Table 2.2, which can be found in Section 2.3. The gasification of pure cellulose was conducted in order to assess the impact of additional catalysts (transition metals on various support materials) added to the process. The catalysts were expected to enhance the total gas yield and to catalyse (i) tar cracking reactions (ii) reforming reactions (steam, dry) and (iii) the water-gas shift reaction.

### 4.2.1 H<sub>2</sub> yield

Figure 4.9 shows the cumulative H<sub>2</sub> yield obtained during decomposition of cellulose with and without additional catalysts in the temperature range 200-600 °C, when the major weight loss occurs (Figure 4.10, right). The yield was calculated using a semi-quantitative system, described in Section 3.3, that did not give the real value of H<sub>2</sub> produced, but was used to compare the various samples.

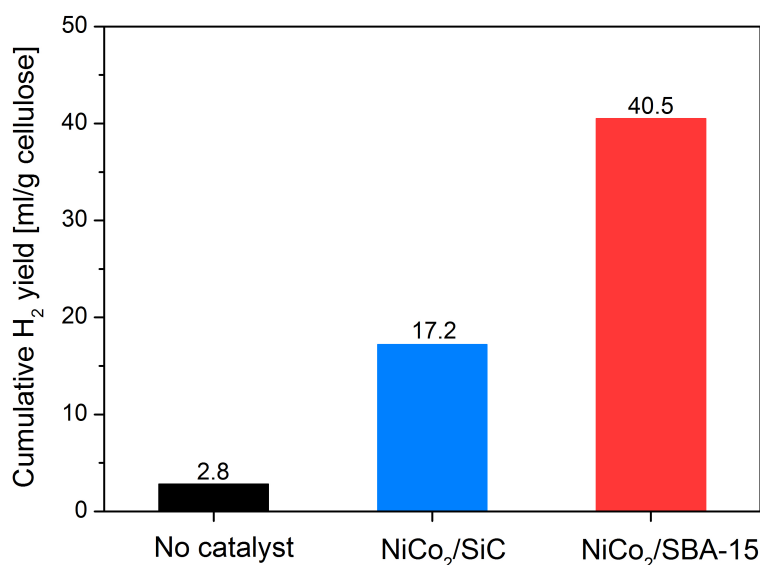


**Figure 4.9** Cumulative H<sub>2</sub> yield obtained between 200-600 °C of cellulose decomposition.

The decomposition of pure cellulose resulted in a hydrogen yield of just 2.8 ml/g cellulose. Considering the total gas yield of 257.8 ml/g cellulose, H<sub>2</sub> made up only 1.0 vol% of the dry gas obtained during the process (Table 4.3). Adding catalysts to the cellulose significantly elevated (i) the hydrogen yield, (ii) the total gas yield and the (iii) share of hydrogen in the dry gas, confirming the impact of the catalysts on the cellulose decomposition. NiCo<sub>2</sub>/SiC increased the total gas yield by almost 20% to 307.2 ml/g cellulose and yielded 17.2 ml/g cellulose of hydrogen, accounting for 5.3 vol% of the dry gas. The SBA-15 supported catalyst showed even better results, elevating the total gas yield to 487.5 ml/g cellulose, the hydrogen yield to 40.5 ml/g cellulose and thus the share of H<sub>2</sub> to 8.2 vol% of the dry gas.

Considering that the active surface area of both catalysts (Table 4.2) was almost the same and that the same phase compound (which was presumably NiCo<sub>2</sub>) [5]) was formed upon reducing the catalysts, the diverging results, can most likely be traced to the different structures of the two support materials. The clearly better results revealed by the SBA-

#### 4 Results and discussion

15 supported catalyst probably arose from its ordered, inner pore structure with a high surface area that was accessible through relatively large pores (5.3 nm according to Table 4.1), and that would have allowed various molecules to enter the inner structure, facilitate mass transfer, and thus increase the residence time and rate of conversion. Furthermore, the interactions of molecules in the inner structure of NiCo<sub>2</sub>/SBA-15 with metal sites deposited on the inner surface may have contributed to the enhanced hydrogen and total gas yield, but were unlikely, according to the results from the chemisorption experiments (Table 4.2), which suggested a poor incorporation of the metal sites into the catalyst.

Catalyst	H <sub>2</sub>	CO	CO <sub>2</sub>	CH <sub>4</sub>	C <sub>x</sub> H <sub>y</sub>	Ald	For	Alc	TGY
Pure cellulose	1.0	42.4	30.0	3.3	6.5	11.1	4.7	1.0	257.8
NiCo <sub>2</sub> /SBA-15	8.2	56.7	27.6	1.5	2.1	3.1	0.3	0.5	487.5
NiCo <sub>2</sub> /SiC	5.3	46.7	40.4	1.5	1.3	3.5	0.8	0.5	307.2

**Table 4.3** Product gas distribution [vol% dry] and total gas yield [ml/g cellulose] obtained between 200-600 °C of cellulose decomposition. (Ald) Aldehydes, (For) Formaldehydes, (Alc) Alcohols, (TGY) Total Gas Yield.

As NiCo<sub>2</sub>/SiC had a very low BET surface area, which was ascribed to the blockage of the pores by the metal sites during impregnation, no access to an inner pore structure was available. Therefore the enhanced gas and hydrogen yield noted in this case presumably resulted only from interactions of molecules with the metal sites located on the outer surface of the catalyst. It should of course be taken into account, that the results could have also been influenced by other factors, like the different surface chemistry of both catalysts, which wasn't examined in this work, or the development of different phases on the the surface of the catalysts during reduction (which could have been assessed using wide-angle X-ray diffraction).

#### 4.2.2 H<sub>2</sub> generation

According to Figure 4.10 (right), all three samples show a similar weight loss profile, starting at 250 °C, peaking at about 395 °C and revealing a sharp decrease just after the peak, which is consistent with literature data for cellulose decomposition [22]. The only difference among the three profiles is the small shoulder exhibited by NiCo<sub>2</sub>/SBA-15 at higher temperatures, indicating that some molecules had not been released from the surface of the catalyst.

Looking at the hydrogen generation rates shown in Figure 4.10 (left), the graphs dedicated to the gasification of cellulose with additional catalysts start at about 330 °C, which

#### 4 Results and discussion

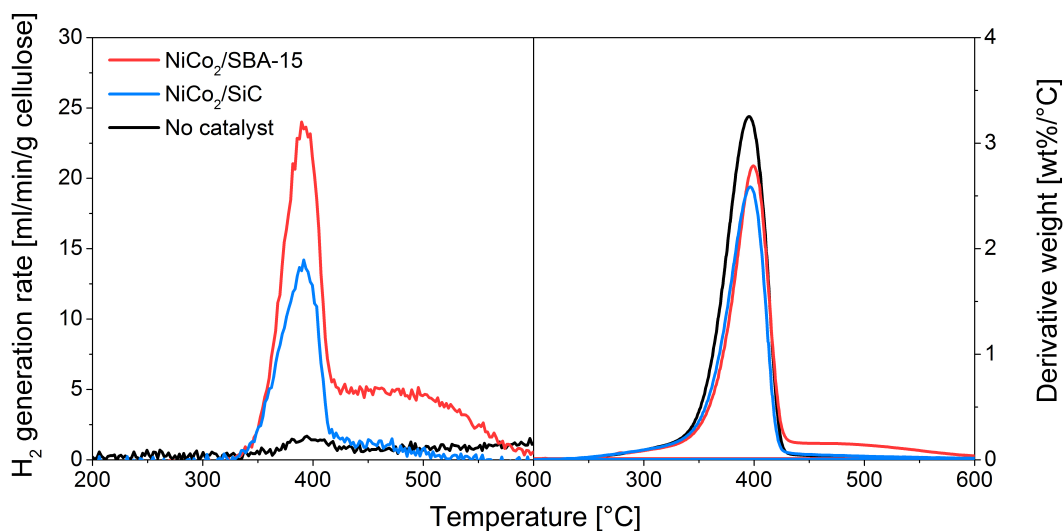
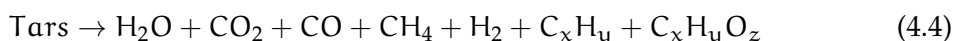


**Figure 4.10** Hydrogen generation (left) and weight loss profile (right) obtained between 200-600 °C of cellulose decomposition.

is 80 °C later than the onset of weight loss. In this early phase of cellulose decomposition mainly H<sub>2</sub>O, CO and CO<sub>2</sub>, but also possible hydrogen sources, like CH<sub>3</sub>CHO (acetaldehydes), CH<sub>2</sub>O (formaldehydes), CH<sub>3</sub>OH (methanols) and tars, evolved from the cellulose, exhibited by their generation-curves in Figures 4.11 and 4.12, which show them beginning to appear as weight loss begins. Nickel-containing catalysts promote cracking reactions (Equations 4.1 - 4.4), as they usually catalyse the rupture of C-C and C-H bonds, and thus improve hydrogen generation commencing parallel to the weight loss. This assumption is supported by the results of Zhao et al. [5, 7], who investigated the influence of supported Ni and Ni-Co catalysts on the hydrogen yield during pyrolysis of cellulose, and found hydrogen generation curves and weight loss profiles starting almost at same temperatures (250 °C) and secondary peaks at around 280 °C. This indicated that cracking reactions, catalysed by the Ni or Ni-Co catalysts, took place mainly inside the pores of the applied catalysts.



As the vigorous argon purge flow made the interactions of molecules and active metal sites located on the outer surface rather unfeasible, and hence they would have most likely taken place in the pores of the catalysts, the lack of hydrogen generation in the

#### 4 Results and discussion

initial phase of cellulose decomposition indicates, that there was either no inner pore structure accessible for the evolved molecules or there were no active sites present inside the pores to react with the penetrated species. The former explanation is consistent with the conclusions made from the characterization of NiCo<sub>2</sub>/SiC, whose inner pore structure was blocked and thus not accessible. The latter explanation would be consistent with the conclusions drawn from the characterization results obtained from NiCo<sub>2</sub>/SBA-15, which suggest a poor incorporation of metal sites into the catalyst.

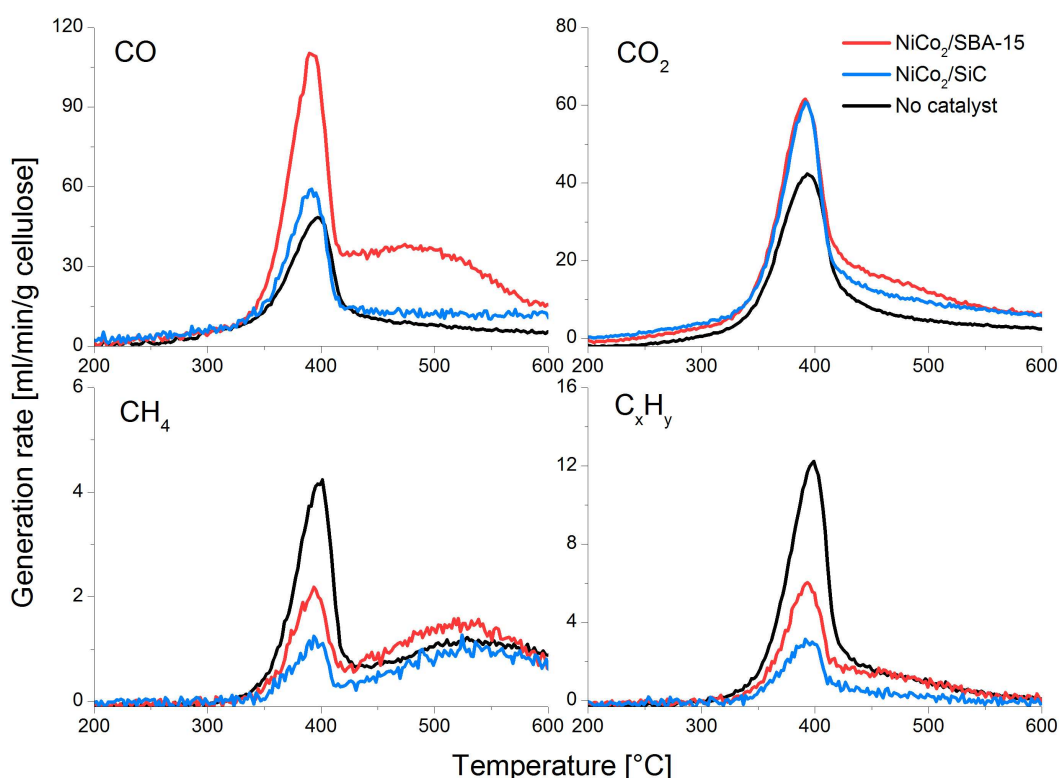


**Figure 4.11** Generation rates of CO, CO<sub>2</sub>, CH<sub>4</sub> and C<sub>x</sub>H<sub>y</sub> obtained between 200-600 °C of cellulose decomposition.

Heating to about 350 °C initiated the period of major weight loss, which terminated at 430 °C, and caused a steep increase in the rate of weight loss and in the generation rates of all species measured during decomposition (Figure 4.11 and 4.12), including CH<sub>4</sub>, C<sub>x</sub>H<sub>y</sub> any H<sub>2</sub>, which did not evolve during the initial phase of the decomposition (between about 250 and 330 °C). The appearance of hydrogen, methane and other hydrocarbons together with the built up of CO<sub>2</sub> and H<sub>2</sub>O and the elevated temperatures made the endothermic reforming reactions, listed below (Equations 4.5 - 4.7), feasible and they are the most probable sources of H<sub>2</sub> over this period.

#### 4 Results and discussion

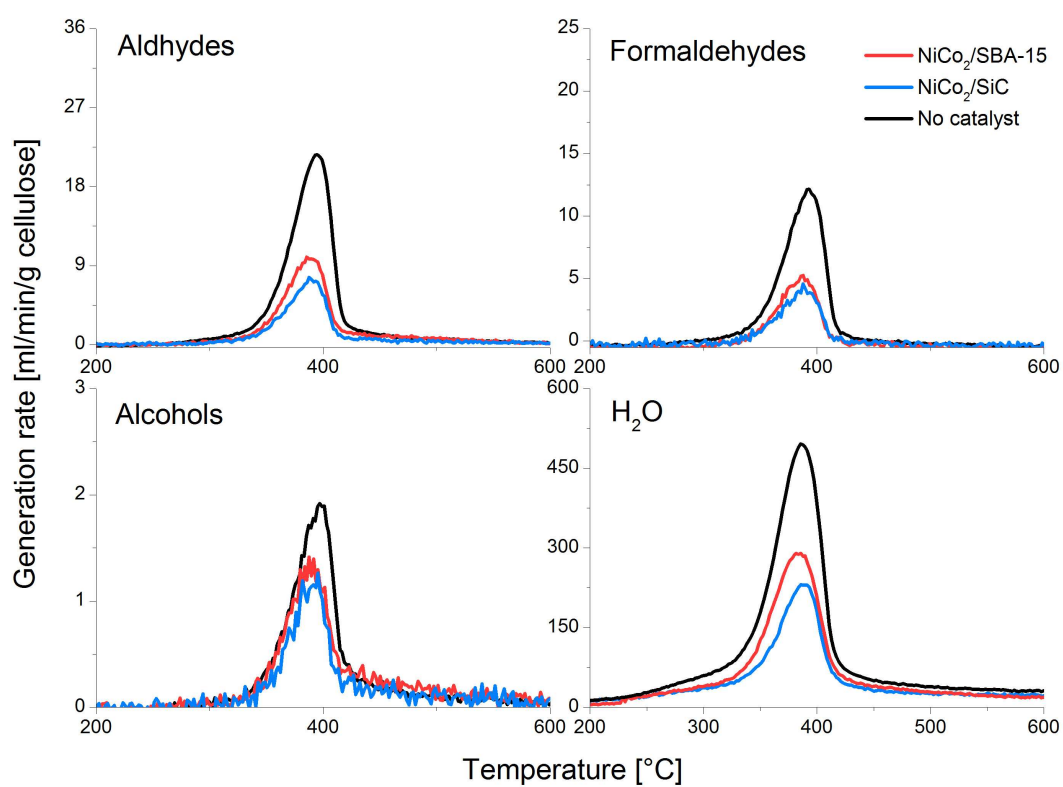
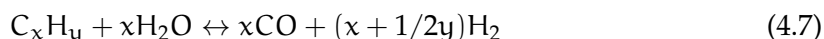


**Figure 4.12** Generation rates of acetaldehydes, formaldehydes, alcohols and H<sub>2</sub>O obtained between 200-600 °C of cellulose decomposition.

#### 4 Results and discussion



Besides reforming reactions, the slightly exothermic water-gas shift reaction (Equation 4.8) and the cracking reactions (Equations 4.1 - 4.4) could have contributed to hydrogen production at this stage of the decomposition, as all species were abundant. This was confirmed by the graphs in Figure 4.13, which show the proportion of the main gaseous species, in vol%, as a function of temperature. In these graphs aldehydes and formaldehydes as well as hydrocarbons and methane were much more prevalent over 350-430 °C for the gasification of pure cellulose than for gasification with additional catalysts. Together with the lower shares of hydrogen and CO exhibited by the diagram for pure cellulose, the occurrence of cracking and reforming reactions can be suggested.

Observing Figure 4.13 in more detail over the considered temperature range, shows that the SBA-15 supported catalyst better catalysed reforming and cracking reactions than SiC-supported one, as the increases in hydrogen and CO proportions are accompanied by a drop of CO<sub>2</sub>. On the other hand, the NiCo<sub>2</sub>/SiC graph exhibits a slight increase of CO<sub>2</sub> and hydrogen but a decrease of CO, which suggests that the water-gas shift reaction was more prominent. This might be related to the porous structure of NiCo<sub>2</sub>/SBA-15, which may be accessible to the molecules evolved during cellulose gasification and thus increased their residence times and conversion rates. The enhanced execution of the water-gas shift reaction supposed for SiC-supported catalyst might be explained by the affinity of Ni-Co catalysts for oxygen-containing species like CO. Apart from the present reaction mechanisms the graphs of both the SBA-15- and the SiC-supported catalysts, show plateaus for the proportion of hydrogen in this period. As the weight loss profile peaks in the same temperature range, this range can be considered as the best for the hydrogen production.

At temperatures higher than 430 °C, a rather sharp drop of the weight-loss profiles as well as in the generation rates of most of the evolved species, was observed for all three samples. Only the generation rates of hydrogen and CO obtained during cellulose gasification with catalysts, revealed shoulders at elevated temperatures (430-550 °C). The shoulders associated with NiCo<sub>2</sub>/SBA-15 are much more distinct than the one associated with NiCo<sub>2</sub>/SiC, and thus connected with a much higher hydrogen yield. The availability of CO and H<sub>2</sub>O, whose generation rates exhibits no shoulders but rather smooth

4 Results and discussion

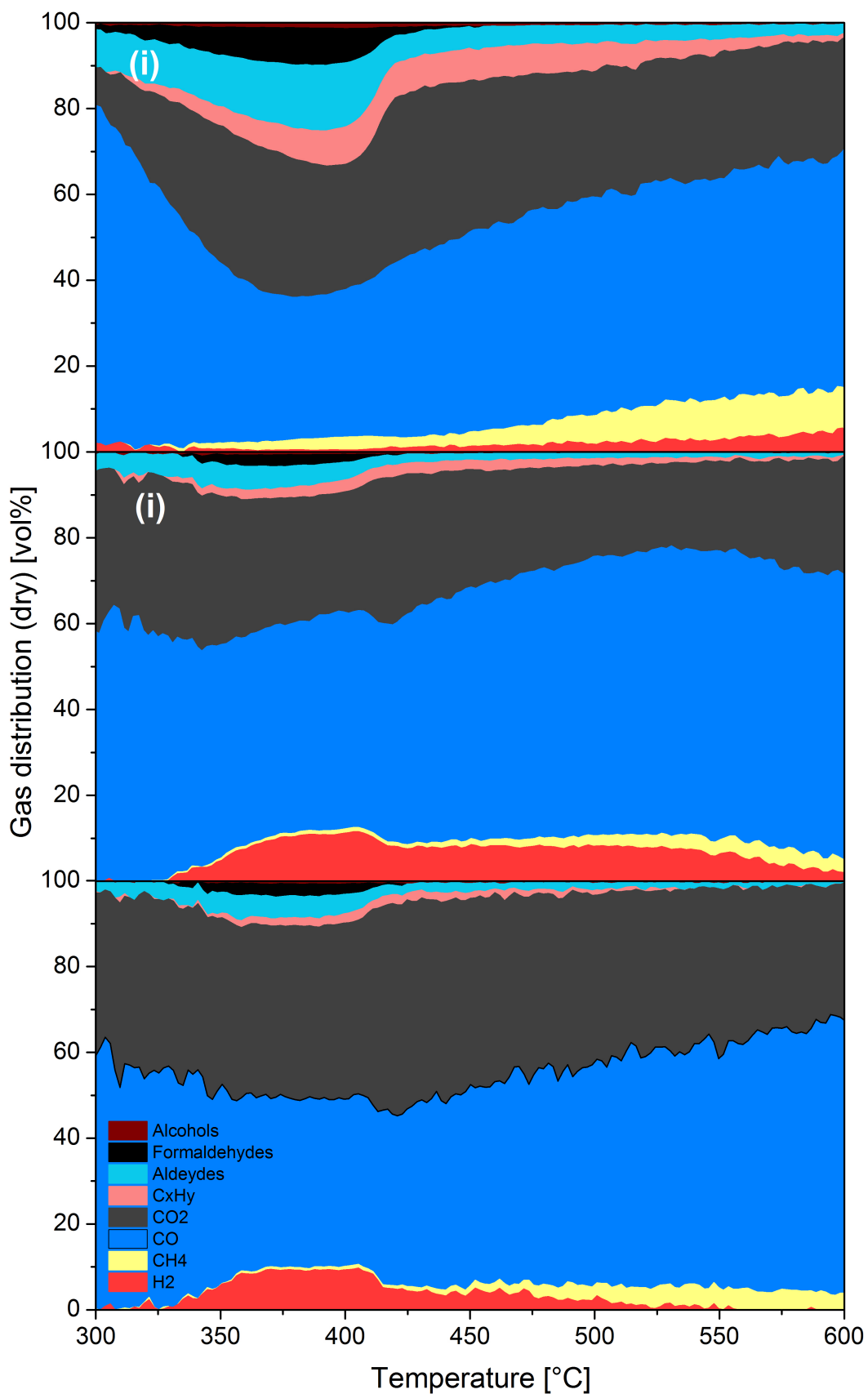
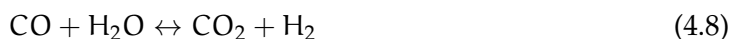


Figure 4.13 Proportions of the main gaseous products (dry) as a function of temperature. (i) pure cellulose, (ii) NiCo<sub>2</sub>/SBA-15, (iii) NiCo<sub>2</sub>/SiC.

#### 4 Results and discussion

decreases, indicates, that the main hydrogen source at elevated temperatures was most likely the water-gas shift reaction.



The sharp drop in the generation rates of aldehydes, formaldehydes and alcohols to almost zero in this temperature range, suggests that the cracking reactions (Equations 4.1 - 4.4) no longer occurred, or that they occurred much more slowly than the subsequent reforming reactions. Some hydrogen formation can be attributed to the reforming reactions, as the generation rates of  $\text{CO}_2$ ,  $\text{CH}_4$  and  $\text{C}_x\text{H}_y$  decreased slowly, meaning that these were available as possible reactants. The shoulder in CO generation might be related to bonding of CO molecules to the metal sites, which could cause CO to dissociate at higher temperatures. This further supports the suggestion made earlier in this section, that Ni-Co catalysts showed affinity for oxygen-containing species like CO and would also explain the lower fraction of CO in the products during the initial stage of the gasification (250-330 °C) when an SBA-15- or SiC-supported catalyst was present (Figure 4.13). The figure further shows a second plateau of  $\text{H}_2$ -share for  $\text{NiCO}_2/\text{SBA-15}$  from about 425-550 °C, indicating the continuous availability of reactants for hydrogen-yielding reactions. This was mainly due to the inner pore structure and the resulting elevated residence time of the penetrated molecules.

### 4.2.3 H<sub>2</sub> selectivity

Figure 4.14 reveals the influence of NiCo<sub>2</sub>/SBA-15 and NiCo<sub>2</sub>/SiC on the distribution of the main gaseous products obtained between 200 and 600 °C of cellulose decomposition. NiCo<sub>2</sub>/SBA-15 and NiCo<sub>2</sub>/SiC enhanced the hydrogen generation significantly, and SBA-15-supported catalyst showed the better H<sub>2</sub> selectivity among the two catalysts (8.2/5.3 vol%, Table 4.3). Both catalysts showed similar shares of acetaldehydes, formaldehydes, alcohols, CH<sub>4</sub> and C<sub>x</sub>H<sub>y</sub>, which were much lower than those obtained from pure cellulose; this further indicated the catalysts' activity for reforming and cracking reactions. The two catalysts differed mainly in their CO/CO<sub>2</sub>-ratios. The SBA-15-supported catalyst showed the highest CO share accompanied by the lowest CO<sub>2</sub> share among the three samples, which suggested its activity in promoting reforming reactions. The SiC-supported catalyst, however, had the highest proportion of CO<sub>2</sub> among all samples, and produced a CO content between the one revealed by pure cellulose and NiCo<sub>2</sub>/SBA-15. This is most likely due to the preference of NiCo<sub>2</sub>/SiC for the water-gas shift reaction rather than reforming reactions.

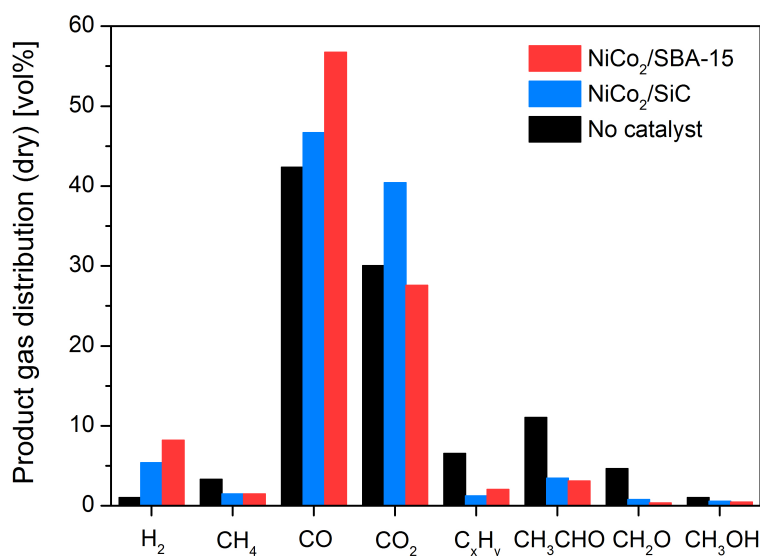


**Figure 4.14** Distribution of the main gaseous products (dry) obtained between 200-600 °C of cellulose decomposition.

## 5 Conclusion and outlook

### 5.1 Conclusion

The synthesis of mesoporous SiC was achieved using mesoporous SBA-15 silica as a template. Despite that the well-ordered structure of the template, its superior BET surface area of 887.4 m<sup>2</sup>, and relatively big pore size of 6.5 nm could not be preserved during the nanocasting process, SiC showed a high surface area of 450.9 m<sup>2</sup>/g and an most common pore size, in the mesoporous range of 3.9 nm. It is assumed that the use of NaOH as the etching agent in order to remove the silica template in the last step of the nanocasting process, caused the loss of order as well as the decrease of surface area.

After impregnating Ni and Co into the SiC, a tremendous drop of the BET surface area to 15.4 m<sup>2</sup>/g, a rather low active metal surface area of 0.89 m<sup>2</sup>/g and an average metal crystal size of 75.6 nm were detected. The BET surface area of the SBA-15-supported catalyst also dropped by more than 400 m<sup>2</sup>/g, upon incorporatin the active metals, and the catalyst had similar values of active surface area and crystallite size (despite its higher BET surface area an pore size). Thus it is supposed that the impregnation of the metals into the pores of the supports mostly failed, and henv e they were deposited on the outer surface of the support materials only, blocking their pores to a high degree.

Despite the appaerent poor impregnation, the SiC-supported catalyst significantly enhanced both, the hydrogen yield and selectivity during the gasification of cellulose in the lab-reactor. The yield increased from 2.8 to 17.2 ml/g cellulose and the selectivity raised from 1.0 to 5.3 vol% indicating the activity of NiCo<sub>2</sub>/SiC for reforming and cracking reactions, as well as the water-gas shift reaction, which was the most favoured among the three groups. From the even higher yield and selectivity produced sing an NiCo<sub>2</sub>/SBA-15 catalyst (40.5 ml/g cellulose, 8.2 vol%), which was more active in catalysing reforming and cracking reactions than NiCo<sub>2</sub>/SiC, it can be concluded that the porous structure played an important role in this context.

Summarized it can be stated, that the elevated hydrogen yield and selectivity revealed by the SiC-supported catalyst, demonstrate the potential of this material, especially, because

## 5 Conclusion and outlook

its suppositionally biggest advantage over other materials, the hydrothermal stability, was not even taken into consideration.

### 5.2 Outlook

An examination of the hydrothermal stability of SiC compared to other, established support materials should be addressed, in order to verify the potential of the material. The synthesis of SiC and the impregnation of the metals into the support, should further be adjusted to yield a SiC-supported catalyst with higher BET and active metal surface area and a better distribution of the metal sites. In this context a change of etching agent should also be considered. Moreover, studies on the reaction mechanisms triggered by the SiC catalyst and the impact of the substrate on the reactions should be made.

Additionally, investigations on the behaviour of SiC- and SBA-15-supported catalysts under conditions closer to reality, e.g. in a fluidized bed gasifier process development unit could be made. Hence, the sensitivity of SiC and SBA-15 on abrasion and coking and the influence of BET and active surface area and pore size on the gasification process, could be assessed.

## 6 Nomenclature

### Variables

$\lambda$	[nm]	Wave length
$\lambda$	[-]	Lambda value aka. Equivalence Ratio ER
$\Theta$	[m/m]	Bragg angle
ACS	[nm]	Average Crystallite Size
APD	[nm]	Average Pore Diameter
ASA	[m <sup>2</sup> /g]	Active Surface Area
d	[nm]	Spacing between the planes in an atomic lattice
ER	[-]	Equivalence Ratio aka. Lambda value
$f_i$	[ml/g]	Generation rate of species i
$\Delta H_{298.15}^0$	[kJ/mol]	Standard enthalpy of formation
$H_i$	[N/m <sup>2</sup> ]	Henry's law constant of component i
$IC_i$	[A]	Ion-current of species with the mass-to-charge ratio i
$IC_{20}$	[A]	Ion-current signal of Argon (mass-to-charge ratio of 20)
$IC_{40}$	[A]	Ion-current signal of Argon (mass-to-charge ratio of 40)
LHV	[kJ/kg]	Lower Heating Value
m	[kg]	Mass of an ion
$m_c$	[g]	Mass of cellulose
MD	[%]	Metal Dispersion
MCV	[ $\mu$ mol/g]	Monolayer Chemisorbed Volume
n	[-]	Integer
$p_{ges}$	[N/m <sup>2</sup> ]	Total pressure of the gas mixture
PV	[cm <sup>3</sup> /g]	Pore Volume
q	[1/nm]	Scattering vector
SA	[m <sup>2</sup> /g]	BET Surface Area
T	[°C]	Temperature
TGY	[ml/g]	Total Gas Yield
$v_{Ar}$	[ml/min]	Flow rate of Argon
$x_i$	[-]	Mole fraction of gas i in solution
$y_i$	[-]	Mole fraction of i-th component in gas-mixture
z	[As]	Number of elementary charges carried by an ion

## Abbreviations

AER	Adsorption Enhanced Reforming
Alc	Alcohols
Ald	Aldehydes
APR	Aqueous Phase Reforming
ATR	Autothermal Reforming
BET	Brunauer-Emmett-Teller (Inventors' names)
BJH	Barrett-Joyner-Halender (Inventors' names)
BP	British Petrol
BSE	Back-Scattered Electrons
CCS	Carbon Capture and Storage
DI Water	Deionized water
DP	Degree of Polymerisation
EHFP	European Hydrogen and Fuel Cell Technology Platform
FCTP	Fuel Cell Technology Program
For	Formaldehydes
HyPr-RING	Hydrogen Production by Reaction Integrated Novel Gasification
IEA	International Energy Agency
IGCC	Integrated Gasification Combined Cycle
IUPAC	International Union of Pure and Applied Chemistry
LCT	Liquid Crystal Templating
MEA	Mono-Ethanol Amine
MS	Mass Spectroscopy
OECD	Organisation of Economic Co-operation and Development
PCMS	Polycarbomethylsilane
PEM	Proton Exchange Membrane
PEMFC	Polymer Electrolyte Membrane Fuel Cell
PO	Partial Oxidation
SAXS	Small Angle X-ray Diffraction
SEM	Scanning Electron Microscopy
SMR	Steam Methane Reforming
SOFC	Solid Oxide Fuel Cell
STP	Standard Temperature and Pressure
TEM	Transmission Electron Microscopy
TEOS	Tetraethylortosilcate
TGA	Thermogravimetry analysis
TGMS	Thermogravimetric analyzer coupled with a mass Spectrometer
WAXS	Wide Angle X-ray Scattering
XRD	X-Ray Diffraction

## References

- [1] A.V. Bridgewater. Renewable fuels and chemicals by thermal processing of biomass. *Chemical Engineering Journal*, 91:87–102, 2003.
- [2] Meng Ni, Dennis Y.C. Leung, Michael K.H. Leung, and K. Sumathy. An overview of hydrogen production from biomass. *Fuel Processing Technology*, 87:461–472, 2006.
- [3] Nicholas H. Florin and Andrew T. Harris. Enhanced hydrogen production from biomass with in situ carbon dioxide capture using calcium oxide sorbents. *Chemical Engineering Science*, 63(2):287 – 316, 2008.
- [4] Y. F. Shi, Y. Meng, D. H. Chen, S. J. Cheng, P. Chen, H. F. Yang, Y. Wan, and D. Y. Zhao. Highly ordered mesoporous silicon carbide ceramics with large surface areas and high stability. *Advanced Functional Materials*, 16(4):561–567, 2006.
- [5] Ming Zhao, Tamara L. Church, and Andrew T. Harris. Sba-15 supported ni-co bimetallic catalysts for enhanced hydrogen production during cellulose decomposition. *Applied Catalysis B: Environmental*, 101(3-4):522 – 530, 2011.
- [6] Ming Zhao, Nicholas H. Florin, and Andrew T. Harris. Mesoporous supported cobalt catalysts for enhanced hydrogen production during cellulose decomposition. *Applied Catalysis B: Environmental*, 97(1-2):142 – 150, 2010.
- [7] Ming Zhao, Nicholas H. Florin, and Andrew T. Harris. The influence of supported ni catalysts on the product gas distribution and h2 yield during cellulose pyrolysis. *Applied Catalysis B: Environmental*, 92(1-2):185 – 193, 2009.
- [8] International Energy Agency. 2011 key world energy statistic. Paris, 2011.
- [9] Enerdata. World energy use in 2010: over 5
- [10] International Energy Agency. World energy outlook 2011 factsheet. Paris, 2011.
- [11] BP. Bp energy outlook 2030. London, 2011.
- [12] Exxon Mobile. A view to 2040. Irving, Texas, 2012.
- [13] International Energy Agency. Iea energy technology essentials: Hydrogen production and distribution, 2007.

## References

- [14] Vijay Ramani. Fuel cells. *The Electrochemical Society Interface*, 15/1:41, 2006.
- [15] General Motors. Well-to-wheels analysis of advanced fuel/vehicles systems, May 2005.
- [16] United States Department of Energy. Hydrogen posture plan - an integrated research, development and demonstration plan, December 2006.
- [17] European Hydrogen and Fuel Cell Technology Platform. Strategic research agenda, July 2005.
- [18] United States Department of Energy, May 2011. <http://www1.eere.energy.gov> (Content Last Update: 10/05/2011).
- [19] United States Department of Energy. Overview of hydrogen and fuel cell budget, February 2011.
- [20] European Hydrogen and Fuel Cell Technology Platform. Budget of the fuel cell and hydrogen joint undertaking for the financial year 2012, January 2012.
- [21] Angela Miltner. *Techno-ökonomische Analyse der regenerativen Produktion von Wasserstoff für den Einsatz in Fahrzeugen*. PhD thesis, Vienna University of Technology, 2010.
- [22] Hermann Hofbauer, Martin Kaltschmitt, and Hans Hartmann. *Energie aus Biomasse*. Hofbauer, Hermann and Kaltschmitt, Martin and Hartmann, Hans, 2009.
- [23] R.R. Davda, J.W. Shabaker, G.W. Huber, R.D. Cortright, and J.A. Dumesic. A review of catalytic issues and process conditions for renewable hydrogen and alkanes by aqueous-phase reforming of oxygenated hydrocarbons over supported metal catalysts. *Appl. Catal. B-Environ*, 56:171–186, 2005.
- [24] Intergovernmental panel on climate change IPCC. Carbon dioxide capture and storage, 2005.
- [25] C Franco, F Pinto, I Gulyurtlu, and I Cabrita. The study of reactions influencing the biomass steam gasification process. *Fuel*, 82(7):835 – 842, 2003.
- [26] Christoph Pfeifer, Stefan Koppatz, and Hermann Hofbauer. Steam gasification of various feedstocks at a dual fluidised bed gasifier: Impacts of operation conditions and bed materials. *Biomass Conversion and Biorefinery*, 1:39–53, 2011. 10.1007/s13399-011-0007-1.
- [27] S. Turn, C. Kinoshita, Z. Zhang, D. Ishimura, and J. Zhou. An experimental investigation of hydrogen production from biomass gasification. *International Journal of Hydrogen Energy*, 23(8):641 – 648, 1998.

## References

- [28] Nicholas H. Florin and Andrew T. Harris. Hydrogen production from biomass coupled with carbon dioxide capture: The implications of thermodynamic equilibrium. *International Journal of Hydrogen Energy*, 32(17):4119 – 4134, 2007.
- [29] Javier Gil, Jose Corella, Maria P. Aznar, and Miguel A. Caballero. Biomass gasification in atmospheric and bubbling fluidized bed: Effect of the type of gasifying agent on the product distribution. *Biomass and Bioenergy*, 17(5):389 – 403, 1999.
- [30] Christoph Pfeifer and Hermann Hofbauer. In-situ co<sub>2</sub>-absorption in a dual fluidized bed biomass steam gasifier to produce a hydrogen rich syngas. *Chemical Engineering Technology*, 32:348–352, 2009.
- [31] Shiyong Lin, Michiaki Harada, Yoshizo Suzuki, and Hiroyuki Hatano. Process analysis for hydrogen production by reaction integrated novel gasification (hypr-ring). *Energy Conversion and Management*, 46(6):869 – 880, 2005.
- [32] Toshiaki Hanaoka, Takahiro Yoshida, Shinji Fujimoto, and Kenji Kamei. Hydrogen production from woody biomass by steam gasification using a co<sub>2</sub> sorbent. *Biomass and Bioenergy*, 28:63–68, 2005.
- [33] Jun Han and Heejoon Kim. The reduction and control technology of tar during biomass gasification/pyrolysis: An overview. *Renewable and Sustainable Energy Reviews*, 12(2):397 – 416, 2008.
- [34] David Sutton, Brian Kelleher, and julian R.H. Ross. Review of literature on catalysts for biomass gasification. *Fuel Processing Technology*, 73:155 – 173, 2001.
- [35] Z. Abu El-Rub, E.A. Bramer, and G. Brem. Review of catalysts for tar elimination in biomass gasification processes. *Ind. Eng. Chem. Res.*, 43:6911–6919, 2004.
- [36] C. Pfeifer, S. Koppatz, and H. Hofbauer. Catalysts for dual fluidised bed biomass gasification - an experimental study at the pilot plant scale. *Biomass Conversion and Biorefinery*, 1:63–74, 2011.
- [37] S. Rapagna, H. Provendier, C. Petit, A. Kiennemann, and P.U. Foscolo. Development of catalysts suitable for hydrogen or syn-gasproduction from biomass gasification. *Biomass and Bioenergy*, 22:377–388, 2002.
- [38] Takeshi Furusawa and Atsushi Tsutsumi. Development of cobalt catalysts for the steam reforming of naphthalene as a model compound of tar derived from biomass gasification. *Applied Catalysis A: General*, 278(2):195 – 205, 2005.

## References

- [39] Jose Corella, Alberto Orío, and Pilar Aznar. Biomass gasification with air in fluidized bed: reforming of the gas composition with commercial steam reforming catalysts. *Ind. Eng. Chem. Res.*, 37:4617–4624, 1998.
- [40] J. Rouquerol. Recommendations for the characterization of porous solids (technical report). *Pure and Appl. Chem.*, 66:1739–1758, 1994.
- [41] G.Q. Lu, G.Q. Lu, and G.X.S. Zhao. *Nanoporous materials: science and engineering*. Series on chemical engineering. Imperial College Press, 2004.
- [42] Avelino Corma. From microporous to mesoporous molecular sieve materials and their use in catalysis. *Chemical Reviews*, 97(6):2373–2420, 1997.
- [43] K.S. Triantafyllidis, E.F. Iliopoulou, and E.V. Antonakou. Catalytic conversion of biomass pyrolysis products by mesoporous materials: Effect of steam stability and acidity of al-mcm-41 catalysts. *Chemical Engineering Journal*, 134:51–57, 2007.
- [44] Ryong Ryoo and Shinae Jun. Improvement of hydrothermal stability of mcm-41 using salt effects during the crystallization process. *The Journal of Physical Chemistry B*, 101(3):317–320, 1997.
- [45] Meilina Widyawati, T. Andrew Harris, and L. Tamara Church. A novel and highly stable cao-sic sorbent for carbon dioxide capture. Manuscript in preparation.
- [46] Dongyuan Zhao, Jianglin Feng, Qisheng Huo, Nicholas Melosh, Glenn H. Fredrickson, Bradley F. Chmelka, and Galen D. Stucky. Triblock copolymer syntheses of mesoporous silica with periodic 50 to 300 angstrom pores. *Science*, 279(5350):548–552, January 1998.
- [47] J. S. Beck, J. C. Vartuli, W. J. Roth, M. E. Leonowicz, C. T. Kresge, K. D. Schmitt, C. T. W. Chu, D. H. Olson, and E. W. and Sheppard. A new family of mesoporous molecular sieves prepared with liquid crystal templates. *Journal of the American Chemical Society*, 114(27):10834–10843, 1992.
- [48] Jeffrey S Beck and James C Vartuli. Recent advances in the synthesis, characterization and applications of mesoporous molecular sieves. *Current Opinion in Solid State and Materials Science*, 1(1):76 – 87, 1996.
- [49] Larry L. Hench and Jon K. West. The sol-gel process. *Chemical Reviews*, 90(1):33–72, 1990.
- [50] Dongyuan Zhao, Qisheng Huo, Jianglin Feng, Bradley F. Chmelka, and Galen D. Stucky. Nonionic triblock and star diblock copolymer and oligomeric surfactant

## References

- syntheses of highly ordered, hydrothermally stable, mesoporous silica structures. *Journal of the American Chemical Society*, 120(24):6024–6036, 1998.
- [51] Dongyuan Zhao, Jinyu Sun, Quanzhi Li, and Galen D. Stucky. Morphological control of highly ordered mesoporous silica sba-15. *Chemistry of Materials*, 12(2):275–279, 2000.
- [52] Piotr Krawiec, Dorin Geiger, and Stefan Kaskel. Ordered mesoporous silicon carbide (om-sic) via polymer precursor nanocasting. *Chemical Communications*, 23:2469–2470, 2006.
- [53] Haifeng Yang and Dongyuan Zhao. Synthesis of replica mesostructures by the nanocasting process. *Journal of Materials Chemistry*, 15:1217–1231, 2005.
- [54] Krijn P. de Jong. *Synthesis of Solid Catalysts*. Wiley-VCH, 2009.
- [55] Stephen Brunauer, Lola S. Deming, W. Edwards Deming, and Edward Teller. On a theory of the van der waals adsorption of gases. *Journal of the American Chemical Society*, 62(7):1723–1732, 1940.
- [56] Elliott P. Barrett, Leslie G. Joyner, and Paul P. Halenda. The determination of pore volume and area distributions in porous substances. i. computations from nitrogen isotherms. *Journal of the American Chemical Society*, 73(1):373–380, 1951.
- [57] K. S. W. Sing, D. H. Everett, R. A. W. Haul, L. Moscou, R. A. Pierotti, J. Rouquerol, and T. Siemieniowska. Reporting physisorption data for gas/solid systems with special reference to the determination of surface area and porosity. *Pure & Appl. Chem.*, 57(4):603–619, 1985.
- [58] W. H. Bragg and W. L. Bragg. The reflection of x-rays by crystals. *Proceedings of the Royal Society of London. Series A*, 88(605):428–438, 1913.
- [59] Vitalij K. Pecharsky and Peter Y. Zavalij. *Fundamentals of Powder Diffraction and Structural Characterization of Materials*. kluwer Academic Publishers, 2003.
- [60] O. Glatter and O. Kratky. *Small Angle X-ray Scattering*. Academic Press, 1982.
- [61] Elizabeth M. Slayter. *Light and electron microscopy*. Cambridge University Press, 1992.
- [62] *Quantachrome Corporation Autosorb-1 Gas Sorption System Manual*.
- [63] Nicholas H. Florin and Andrew T. Harris. Screening cao-based sorbents for co<sub>2</sub> capture in biomass gasifiers. *Energy & Fuels*, 22(4):2734–2742, 2008.

## References

- [64] Nicholas H. Florin and Andrew T. Harris. Mechanistic study of enhanced h<sub>2</sub> synthesis in biomass gasifiers with in-situ co<sub>2</sub> capture using cao. *AIChE Journal*, 54(4):1096–1109, 2008.
- [65] James Barker. *Mass Spectrometry: Analytical Chemistry by Open Learning*. Wiley, 1998.

# List of Figures

2.1	Global primary energy demand in Mtoe between 1965-2040 based on Exxon's energy outlook 2011 [12]. (* including biofuels) . . . . .	10
2.2	Current and projected (2020-2030) hydrogen production costs, sensitive to technologies, dependent on assumed energy prices. Re-drawn from reference [13]. . . . .	21
3.1	Possible mechanistic pathways of the formation of SBA-15: (1) liquid crystal phase initiated and (2) silicate anion initiated. Re-drawn from reference [47]. . . . .	36
3.2	Setup of the SBA-15 synthesis. . . . .	38
3.3	Synthesis of ordered mesoporous (OM) SiC using the nanocasting process. Re-drawn from reference [53]. . . . .	39
3.4	Heating programme of SBA-15/PCMS pyrolysis. . . . .	40
3.5	Setup of SBA-15/SiC etching. . . . .	41
3.6	TGMS used for the testing of the catalysts. Right: TGA in closed position with connected MS; Left: opened TGA. . . . .	47
4.1	Adsorption-desorption isotherms of the SBA-15 substrate (left), and the bimetallic NiCo <sub>2</sub> /SBA15 catalyst (right). . . . .	49
4.2	Adsorption-desorption isotherms of the SiC substrate (left) and the bimetallic NiCo <sub>2</sub> /SiC catalyst (right). . . . .	50
4.3	Classification of adsorption-desorption isotherms (left) and hysteresis loops (right) according to the IUPAC. Reproduced from reference [57]. . . . .	51
4.4	Small-angle X-ray diffraction patterns of the blank supports, SBA-15 (left) and SiC (right). . . . .	52
4.5	Transmission electron microscopy images of the blank supports and the reduced catalysts: (i) and (ii) SBA-15, (iii) NiCo <sub>2</sub> /SBA-15, (iv) and (v) SiC, (vi) NiCo <sub>2</sub> /SiC. . . . .	53
4.6	Scanning electron microscopy images of the blank supports and the reduced catalysts: (i) SBA-15, (ii) NiCo <sub>2</sub> /SBA-15, (ii) SiC, (iv) NiCo <sub>2</sub> /SiC. . .	54
4.7	Scanning electron microscopy images of as-synthesized NiCo <sub>2</sub> /SiC: (i) before etching, (ii) after etching. . . . .	55

*List of Figures*

4.8	Scanning electron microscopy images of the reduced catalysts: (i) NiCo <sub>2</sub> /SBA-15, (ii) NiCo <sub>2</sub> /SiC. . . . .	55
4.9	Cumulative H <sub>2</sub> yield obtained between 200-600 °C of cellulose decomposition. . . . .	57
4.10	Hydrogen generation (left) and weight loss profile (right) obtained between 200-600 °C of cellulose decomposition. . . . .	59
4.11	Generation rates of CO, CO <sub>2</sub> , CH <sub>4</sub> and C <sub>x</sub> H <sub>y</sub> obtained between 200-600 °C of cellulose decomposition. . . . .	60
4.12	Generation rates of acetaldehydes, formaldehydes, alcohols and H <sub>2</sub> O obtained between 200-600 °C of cellulose decomposition. . . . .	61
4.13	Proportions of the main gaseous products (dry) as a function of temperature. (i) pure cellulose, (ii) NiCo <sub>2</sub> /SBA-15, (iii) NiCo <sub>2</sub> /SiC. . . . .	63
4.14	Distribution of the main gaseous products (dry) obtained between 200-600 °C of cellulose decomposition. . . . .	65

## List of Tables

2.1	Hydrogen energy system infrastructure elements and key hurdles [16]. . .	14
2.2	Main heterogeneous (i)-(v) and homogeneous (vi)-(ix) reactions occurring during biomass gasification. $\Delta H_{298.15}^0$ in kJ/mol stands for the standard enthalpy of formation. (-) indicates exothermic, (+) endothermic reactions.	22
2.3	Summary of catalysts used as primary measures in biomass gasification processes comparing their advantages and disadvantages [35]. . . . .	30
3.1	Key molecular ions/ion fragments and probable representative molecules [7]. . . . .	48
4.1	Physisorption results of blank support materials and catalysts. (SA) BET Surface Area, (PV) Pore Volume, (APD) Average Pore Diameter. * main peak, ** secondary peak, *** small, indistinct peak, no dominant pore size. . . . .	50
4.2	Chemisorption results of the catalysts. (T) Temperature of chemisorption measurement, (ACS) Average Crystallite Size, (MCV) Monolayer Chemisorbed Volume, (ASA) Active Surface Area, (MD) Metal dispersion. . . . .	56
4.3	Product gas distribution [vol% dry] and total gas yield [ml/g cellulose] obtained between 200-600°C of cellulose decomposition. (Ald) Aldehydes, (For) Formaldehydes, (Alc) Alcohols, (TGY) Total Gas Yield. . . . .	58